ISSN 0915-633X

NATIONAL INSTITUTE FOR FUSION SCIENCE

Three-dimensional Simulation Study of Compact Toroid Plasmoid Injection into Magnetized Plasmas

Y. Suzuki, T-H. Watanabe, T. Sato and T. Hayashi

(Received - Apr. 26, 1999)

NIFS-596 Apr. 1999

This report was prepared as a preprint of work performed as a collaboration reserch of the National Institute for Fusion Science (NIFS) of Japan. This document is intended for infomation only and for future publication in a journal after some rearrangements of its contents.

Inquiries about copyright and reproduction should be addressed to the Research Information Center, National Institute for Fusion Science, Oroshi-cho, Toki-shi, Gifu-ken 509-02 Japan.

RESEARCH REPORT
NIFS Series

NAGOYA, JAPAN

Three-dimensional Simulation Study of Compact Toroid Plasmoid Injection into Magnetized Plasmas

Y. SUZUKI [1], T-H. WATANABE, T. SATO, T. HAYASHI

Theory and Computer Simulation Center, National Institute for Fusion Science, Toki, Gifu, 509-5292, Japan

ABSTRACT. Three-dimensional dynamics of a compact toroid (CT) plasmoid, which is injected into a magnetized target plasma region is investigated by using magnetohydrodynamic (MHD) numerical simulations. It is found that the process of the CT penetration into this region is much more complicated than what has been analyzed so far by using a conducting sphere (CS) model. The injected CT suffers from a tilting instability, which grows with the similar time scale as the CT penetration. The instability is accompanied by magnetic reconnection between the CT magnetic field and the target magnetic field, which disrupts the magnetic configuration of the CT. Magnetic reconnection plays a role to supply the high density plasma initially confined in the CT magnetic field into the target region. Also, the penetration depth of the CT high density plasma is examined. It is shown to be shorter than that estimated from the CS model. The CT high density plasma is decelerated mainly by the Lorentz force of the target magnetic field, which includes not only the magnetic pressure force but also the magnetic tension force. Furthermore, by comparing the CT plasmoid injection with the bare plasmoid injection, magnetic reconnection is considered to relax the magnetic tension force, that is the deceleration of the CT plasmoid.

Keywords: fueling, compact toroid (CT), magnetic reconnection, MHD simulation

1 Introduction

Aiming at steady state operation of a fusion reactor, several fueling schemes have been developed. The compact toroid (CT) plasmoid injection has been considered as one of advanced methods for deep fueling, since the injection velocity of fuel by this scheme is much higher than that by any other schemes. So far, the CT injection method has been discussed in several experiments [1, 2, 3, 4, 5, 6] and theoretical models [7, 8, 9]. In these studies the penetration depth of the CT has been analyzed mainly by using a conducting sphere (CS) model: In this model, the penetration depth is estimated from that of an incompressible, perfectly conducting sphere injected into a vacuum region in which the magnetic field increases along the injection direction [4]. Thus, the injected CS is decelerated by the magnetic pressure force. In other words, the CS can penetrate until the initial CS kinetic energy is exceeded by the magnetic energy required to exclude the magnetic field from the CS volume:

$$\frac{1}{2}\rho V^2 v > \frac{1}{2\mu_0} B^2 v \ . \tag{1}$$

where ρ, V, v, and B is the CS density, the CS injection velocity, the CS volume, and the strength of the target magnetic field at the point where the CS is penetrating, respectively. In TdeV experiments [2, 3], fueling by the CT injection is accomplished without any adverse perturbation to the tokamak discharge. Also, the penetration depth of the CT is 0.6 times as long as the minor radius of TdeV and is well agreement with that estimated from the CS model. However, the size of the CT is $0.12 - 0.30$cm, which is the similar scale as the minor radius of TdeV, that is 0.27cm. It means that deep fueling to reactor grade devices has not been well understood. Also, the dynamics of the injected CT has not been well observed. Our main objective is to understand the dynamics of the injected CT as well as the possibility of deep fueling to reactor grade devices. To achieve this, we investigate three-dimensional dynamics of a CT which is accelerated in the injection region and is injected into the target plasma by using magnetohydrodynamic (MHD) numerical simulations.

2 Simulation Model

The simulation model is the same as that in our previous papers [10, 11]. In the simulation, we use cylindrical coordinates (r, θ, z). The simulation region is composed of two cylinders which connect with each other (Figure 1). One with a smaller radius L_r corresponds to the injection region and the other with a larger radius $4L_r$ corresponds to the target region. The injection region and the target region correspond to a CT gun region and a part of a fusion device, respectively. Lengths of these cylinders are both $L_z/2$. The relative lengths of the sizes are given by $L_r : L_z = 1 : 16$. We employ a perfectly conducting wall for the boundary condition.

The governing equations are given by MHD equations:

$$\frac{\partial \rho}{\partial t} = -\nabla \cdot (\rho \boldsymbol{V}) \ , \tag{2}$$

[1]The present address is the Naka Fusion Research Establishment, Japan Atomic Energy Research Institute, Naka, Ibaraki, 311-0193, Japan.

$$\frac{\partial \rho \boldsymbol{V}}{\partial t} = -\nabla \cdot \rho \boldsymbol{V}\boldsymbol{V} + \boldsymbol{J} \times \boldsymbol{B} - \nabla P - \nabla \cdot \Pi \ , \quad (3)$$

$$\frac{\partial \boldsymbol{B}}{\partial t} = -\nabla \times \boldsymbol{E} \ , \quad (4)$$

$$\frac{\partial P}{\partial t} = -\nabla \cdot (P\boldsymbol{V} - \kappa \nabla T) - (\gamma - 1)(P \nabla \cdot \boldsymbol{V} + \Pi : \nabla \boldsymbol{V} - \eta J^2) \ , \quad (5)$$

$$\boldsymbol{E} = -\boldsymbol{V} \times \boldsymbol{B} + \eta \boldsymbol{J} \ , \quad (6)$$

$$\boldsymbol{J} = \nabla \times \boldsymbol{B} \ , \quad (7)$$

$$T = P/\rho \ , \quad (8)$$

$$\Pi = \nu[\frac{2}{3}(\nabla \cdot \boldsymbol{V})\mathsf{I} - \nabla \boldsymbol{V} -^t (\nabla \boldsymbol{V})] \ . \quad (9)$$

These equations have a non-dimensional form, in which the density, the magnetic field, the velocity, the length, and the time are normalized by one-tenth of the maximum CT density $\rho_0(\equiv 0.1\rho_{\rm CT})$, the maximum strength of the CT magnetic field $B_0(\equiv B_{\rm CT})$, the characteristic Alfvén velocity $V_A(\equiv B_0/\sqrt{\mu_0\rho_0})$, the scale of the cylinder radius L_r, and the Alfvén transit time $\tau_A(\equiv L_r/V_A)$, respectively. The resistivity η, the viscosity ν, and the conductivity κ are fixed to 1.0×10^{-3} in the normalized unit $\mu_0 L_r V_A$, $\rho_0 L_r V_A$, and $k\rho_0 L_r V_A$, respectively.

The initial magnetic configuration is calculated as follows: The toroidal current J_θ of a cylindrical spheromak solution [12] whose radius and length are respectively L_r and $2L_r$ is located in the injection region. Its center is $(r, z) = (0, 6L_r)$. From J_θ, the toroidal component of the vector potential A_θ, and thus the magnetic field is calculated. Furthermore, the current free target magnetic field $B_{\rm target}$, whose strength is an almost uniform and direction is perpendicular to the injection direction is superposed. The CT toroidal magnetic field, the CT poloidal magnetic field, and the target magnetic field are respectively directed as shown in figure 1. The density profile is given by the function of the CT poloidal flux $\psi_{\rm pol} \equiv rA_\theta$,

$$\rho = \rho_{\rm target} + (\rho_{\rm CT} - \rho_{\rm target})\frac{|\psi_{\rm pol}|}{|\psi_{\rm axis}|} \ , \quad (10)$$

where $\psi_{\rm axis}$ is the poloidal flux on the CT magnetic axis. The target plasma density $\rho_{\rm target}$ is assumed to be one percent of the peak CT plasma density $\rho_{\rm CT}$. The pressure is initially uniform ($P_{\rm com} = P_{\rm target} = P_{\rm CT}$). The CT is injected into the target region after acceleration up to the maximum velocity $V_{\rm CT}$ at $t = t_{\rm off} \equiv 2L_r/V_{\rm CT}$. Until this time, the acceleration term, $f_{\rm acc} = \alpha\rho\frac{d}{dt}\left[\frac{1}{2}V_{\rm CT}\{1 - \cos(\frac{\pi}{t_{\rm off}}t)\}\right]$ is added to the z component of the equation of motion. α is given as follows:

$$\begin{cases} \alpha = 1 & \text{for } \rho > \rho_{\rm c} \\ \alpha = 0 & \text{for } \rho \le \rho_{\rm c} \ , \end{cases} \quad (11)$$

where $\rho_{\rm c} \equiv \rho_{\rm target} + 0.2(\rho_{\rm CT} - \rho_{\rm target})$. Namely, the acceleration is done for $\rho > \rho_{\rm c}$ (hereafter, we call it the CT region).

We carry out four simulation runs as shown in Table 1. The explicit finite difference method with second-order accuracy and the Runge-Kutta-Gill method are used to solve the basic equations numerically. Also, the smoothing is applied to the density, the pressure, and the momentum, when the density or the pressure at any point are respectively lower than two percent of the target plasma density or the target plasma pressure ($\rho < 0.02\rho_{\rm target}$ or $P < 0.02P_{\rm target}$). The smoothing function is $f_i = Cf_i + (1 - C)(f_{i-1} + f_{i+1})/2$, where $C = 0.9$ and is employed in r, θ, and z directions. In the case 1 and the case 3, the smoothing does not work because the density and the pressure are not less than each threshold. In the case 2 and the case 4, the smoothing works under above situation. Even so, the smoothing would not change the simulation results so much, because the total energy in the simulation region is almost conserved. The difference between the total energy and the sum of the input and output energy is up to about 3 %.

3 Simulation Results

3.1 Three-dimensional Dynamics of Injected CT

Figure 2 shows the spatial structure of the magnetic flux and the density profile in the case 1 ($B_{\rm target} = 0$) at $t = 0, 20, 40$, and $60\tau_A$. The CT initially put in the injection region ($t = 0\tau_A$) penetrates into the target region ($t = 20$ and $40\tau_A$) and reaches the opposite wall by $t = 60\tau_A$. Through this process, the high density plasma is well confined in the magnetic flux.

Figure 3 shows the spatial structure of magnetic field lines and the high density plasma in the case 2 ($B_{\rm target} = 0.1$) at $t = 0, 20, 40$, and $60\tau_A$. At $t = 20\tau_A$, the high density plasma confined in the CT magnetic field penetrates into the target region. While at $t = 40$ and $60\tau_A$, the high density plasma continues to penetrate there, the magnetic configuration of the CT is almost disrupted. In this process, the injected CT suffers from a tilting instability. Figure 4 shows density contours viewed from the same direction. Initially the density profile is symmetric. At $t = 20\tau_A$, however, the CT plasma tilts to align its magnetic moment with the direction of the target magnetic field [13, 14]. At $t = 40$ and $60\tau_A$, its angle reaches almost 90 degree. The tilting instability is accompanied by magnetic reconnection between the CT magnetic field and the target magnetic field. Figure 5 shows the magnetic structure at $t = 20\tau_A$ viewed from several directions. While the CT excludes some target magnetic field lines expected by the CS model, other magnetic field lines in front of the

CT are reconnected with CT magnetic field lines. Magnetic reconnection plays a role to supply the high density plasma which is initially confined in the CT magnetic field into the target region.

Next, we examine the penetration depth of the CT high density plasma, which is defined by,

$$L_{\rm p} = \int \langle V \rangle \, dt - L_z/2 \ , \quad \langle V \rangle = \sqrt{\frac{\int_{\rho > \rho_c} \rho V^2 dv}{\int_{\rho > \rho_c} \rho dv}} \quad (12)$$

In figure 6 the time evolution of penetration depths in the case 1 and the case 2 is shown. Until about $t = 7\tau_A$, the CT high density plasma in these cases is accelerated in the injection region. After that, it has entered the target region until about $t = 13\tau_A$, and then it penetrates with time. However, after it has entered, the penetration depth in the case 2 becomes gradually shorter than that in the case 1.

3.2 Deceleration Mechanism of CT

3.2.1 Null Target Magnetic Field Case

Before discussing the difference of the penetration depth between the case 1 ($B_{\rm target} = 0$) and the case 2 ($B_{\rm target} = 0.1$), we compare the penetration depth in the case 1 with that of the CS calculated by using the same parameters as the simulation. In figure 6, the penetration depth of the CS with null target magnetic field is also plotted. It is obvious that after stopping the acceleration ($t > t_{\rm off}$) the CS penetrates with no deceleration. On the other hand, the penetration depth in the case 1 becomes shorter than that of the CS. It is considered that in the simulation the target region as well as the injection region is filled with the plasma, which causes the deceleration of the CT. Nevertheless, to understand it in detail. the time evolution of the CT kinetic energy and its energy conversion is examined.

Figure 7 shows the time evolution of the CT kinetic energy and the CS kinetic energy. Until about $t = 6\tau_A$, the CT kinetic energy well coincides with the CS kinetic energy. After that, however, it becomes smaller with time. Figure 8 shows the schematic diagram of energy conversion processes between the kinetic, the magnetic, and the thermal energy, which are divided into the CT region ($\rho > \rho_c$) and the background region ($\rho \leq \rho_c$). From the MHD equations (2) to (9) we use, the energy conversion rates between each energy are easily derived as follows [15]:

$$\frac{dE_{\rm k}}{dt} = -\dot{\varepsilon}^{\rm v}_{\rm k\to t} - \dot{\varepsilon}^{\rm c}_{\rm k\to t} - \dot{\varepsilon}_{\rm k\to m} + \dot{\varepsilon}^{\rm input}_{\rm k} \ , \quad (13)$$

$$\frac{dE_{\rm m}}{dt} = -\varepsilon_{\rm m\to t} + \dot{\varepsilon}_{\rm k\to m} \ , \quad (14)$$

$$\frac{dE_{\rm t}}{dt} = \dot{\varepsilon}^{\rm v}_{\rm k\to t} + \dot{\varepsilon}^{\rm c}_{\rm k\to t} + \dot{\varepsilon}_{\rm m\to t} - \dot{\varepsilon}^{\rm output}_{\rm t} \ , \quad (15)$$

where

$$E_{\rm k} = \frac{1}{2}\int \rho V^2 dv \ , \quad (16)$$

$$E_{\rm m} = \frac{1}{2}\int B^2 dv \ , \quad (17)$$

$$E_{\rm t} = \int \frac{P}{\gamma - 1} dv \ , \quad (18)$$

$$\dot{\varepsilon}^{\rm v}_{\rm k\to t} = \int \boldsymbol{V} \cdot \nabla \cdot \Pi dv \ . \quad (19)$$

$$\dot{\varepsilon}^{\rm c}_{\rm k\to t} = \int \boldsymbol{V} \cdot \nabla P dv \ , \quad (20)$$

$$\dot{\varepsilon}_{\rm k\to m} = -\int \boldsymbol{V} \cdot \boldsymbol{J} \times \boldsymbol{B} dv \ , \quad (21)$$

$$\dot{\varepsilon}_{\rm m\to t} = \int \eta J^2 dv \ . \quad (22)$$

$\dot{\varepsilon}^{\rm input}_{\rm k}$ is the rate of the input kinetic energy, which is given by,

$$\dot{\varepsilon}^{\rm input}_{\rm k} = \int V_z f_{\rm acc} dv \ , \quad (23)$$

and corresponds to the acceleration of the CT. $\dot{\varepsilon}^{\rm output}_{\rm t}$ is the rate of the output thermal energy, which is given by,

$$\dot{\varepsilon}^{\rm output}_{\rm t} = \int \frac{1}{\gamma - 1} \kappa \nabla T \cdot d\boldsymbol{s} \ , \quad (24)$$

where the notation s means the boundary surface of the system, and the vector $\boldsymbol{s}$ orients to the outward and normal direction on the boundary. The conversion rates $\dot{\varepsilon}^{\rm v}_{\rm k\to t}$, $\dot{\varepsilon}^{\rm c}_{\rm k\to t}$, $\dot{\varepsilon}_{\rm k\to m}$, and $\dot{\varepsilon}_{\rm m\to t}$ which respectively represent the viscous heating, the compressional heating, the Lorentz force effect, and the Joule heating, are also divided to the CT region ($\rho > \rho_c$) and the background region ($\rho \leq \rho_c$). The conversion rates $\dot{\varepsilon}^{\rm CT\to back}_{\rm k}$, $\dot{\varepsilon}^{\rm CT\to back}_{\rm m}$, and $\dot{\varepsilon}^{\rm CT\to back}_{\rm t}$ shown in figure 8 correspond to the outflow of each energy from the CT region to the background region. Thus, there exist four energy conversion processes for the CT kinetic energy: the compressional heating, the viscous heating, the Lorentz force effect, and the outflow to the background region. Figure 9 shows the time history of these conversion rates. We can see that the CT kinetic energy is converted mainly by the compressional heating. The peak at $t = 7\tau_A$ in this process is caused by the acceleration of the CT. The small peak at $t = 13\tau_A$ corresponds to the entrance of the CT into the target region. (The peak at $t = 48\tau_A$ is caused by the arrival of the CT to the opposite wall.) Also, the CT kinetic energy is partly converted by the outflow to the background region. Since in the acceleration process the kinetic energy flows into the CT region. its conversion rate becomes negative between about $t = 3\tau_A$ and $5\tau_A$. However, after that, the

kinetic energy flows from the CT region to the background region. The energy conversion by the Lorentz force effect is small but converts the CT kinetic energy to the CT magnetic energy. It is because the force free equilibrium of the CT magnetic configuration is modulated when the CT penetrates with the high velocity,

We can see that the compressional heating is the dominant process to decelerate the CT which is injected into the target region with null magnetic field. However, it depends on the plasma pressure $P_{\rm com}$, which is initially assumed to be constant both in the injection region and the target region. For higher $P_{\rm com}$, the compressional heating becomes more effective [11]. It suggests that the injection velocity of the CT must be faster to penetrate into the higher temperature plasma region.

3.2.2 Case with Target Magnetic Field

The CS model predicts that when there exists the target magnetic field, the injected CS is decelerated by the magnetic pressure force, which leads to the shorter penetration depth than in the null target magnetic field case. In figure 6 the penetration depth of the CS with $B_{\rm target} = 0.1$ is also plotted. Since the strength of the target magnetic field is not so large, the difference of the penetration depth between cases with and without the target magnetic field is small. In figure 10 such differences both in the CS model and the simulation are plotted. From this figure, we can see that the difference in the simulation is larger than in the CS model. It means that the CT injected into the magnetized target plasma is more decelerated than predicted by the CS model. Therefore, in order to consider why such a deceleration is caused, we examine the time evolution of the CT kinetic energy and its energy conversion in the case 2 as in the previous section.

In figure 7, the time evolution of the CS kinetic energy and CT kinetic energy with $B_{\rm target} = 0.1$ is also plotted. Since the injected CS suffers from the deceleration only when it enters the target region, after it has entered the CS kinetic energy keeps a constant value. On the other hand, the CT kinetic energy in the case 2 becomes smaller with time than in the case 1. In figure 11, the difference of the CT kinetic energy between the case 1 and the case 2 is plotted by a solid line and that of the CS kinetic energy between cases with $B_{\rm target} = 0$ and with $B_{\rm target} = 0.1$ is plotted by a broken line. Until the CT has entered in the target region (about $t = 13\tau_A$), the decrease in the simulation is similar to that in the CS model. After that, however, it becomes larger. Figure 12 shows the difference of the energy conversion rates between the case 1 and the case 2. We can see that the compressional heating is dominant and continues to convert the CT kinetic energy through the penetration process. As a result, the decrease of the CT kinetic energy which is due to the existence of the target magnetic field is larger than that estimated from the CS model.

Figure 13 shows the resultant energy difference and the converted energy between $t = 7\tau_A$ and $t = 40\tau_A$ by subtracting those in the case 1 from in the case 2. We can see that firstly the CT kinetic energy is converted to the CT thermal energy through the compressional heating, secondary the CT thermal energy flows into the background region, thirdly the background thermal energy is converted to the background kinetic energy through the compressional heating, and finally the kinetic energy is converted to the magnetic energy by the Lorentz force effect in the background region. Since the background magnetic energy corresponds to the magnetic energy of the target magnetic field, the CT kinetic energy is finally converted to the magnetic energy of the target magnetic field. Therefore, the CT is successively decelerated by the Lorentz force of the target magnetic field through the compressibility of plasma, by which the CT penetration depth becomes shorter than estimated from the CS model.

3.2.3 Null CT Magnetic Field Case

It is considered that in real experiments the CT magnetic field is essential to accelerate the CT plasmoid in the gun region and also to prevent its diffusion. However, in order to examine the Lorentz force effect in detail, we carry out the simulation where a bare plasmoid with null CT magnetic field is injected into the target region. Figure 14 shows the color contour of the density profile in the case 3 ($B_{\rm CT} = 0, B_{\rm target} = 0$). In this case, simulation parameters are the same as those in the case 1 except the strength of the CT magnetic field. We can see that the high density plasma can penetrate into the target region and reaches the opposite wall by $t = 40\tau_A$. Figure 15 shows the spatial structure of magnetic field lines and the high density plasma in the case 4 ($B_{\rm CT} = 0, B_{\rm target} = 0.1$). In this case, also, the high density plasma penetrates into the target region. These results are similar to those with the CT magnetic field. In figure 10, the difference of the penetration depth between the case 3 and the case 4 is plotted. And, in figure 11, the difference of the bare plasmoid kinetic energy between the case 3 and the case 4 is plotted. These are not so different from those with the CT magnetic field. From these results, it is considered that the bare plasmoid which is injected into the magnetized target plasma region is also decelerated by the Lorentz force of the target magnetic field. Thus, we examine the Lorentz force effect in the bare plasmoid injection. The

Lorentz force is divided into two effects: the magnetic pressure force and the magnetic tension force. Therefore, the energy conversion rate for the Lorentz force effect is divided as follows:

$$\dot{\varepsilon}_{k\to m} = \dot{\varepsilon}^{p}_{k\to m} + \dot{\varepsilon}^{t}_{k\to m} \ . \tag{25}$$

where

$$\dot{\varepsilon}^{p}_{k\to m} = -\int \boldsymbol{V}\cdot\nabla(B^2/2)dv \ . \tag{26}$$

$$\dot{\varepsilon}^{t}_{k\to m} = \int \boldsymbol{V}\cdot(\boldsymbol{B}\ \ \nabla)\boldsymbol{B}dv \ . \tag{27}$$

In the bare plasmoid injection, it is easy to divide the Lorentz force effect of the target magnetic field into these two effects. (In the CT plasmoid injection, it is difficult, since magnetic reconnection between the CT magnetic field and the target magnetic field takes place as shown in the previous section.) Figure 16 shows the time evolution of the magnetic pressure force effect and the magnetic tension force effect in the case 4 Until the bare plasmoid has entered the target region, the magnetic pressure force dominantly changes the background kinetic energy to the background magnetic energy. After that, however, while it decreases with time, the magnetic tension force effect increases. The injected bare plasmoid suffers from the magnetic pressure force until it has entered the target region as predicted by the CS model. After that, however, it is decelerated by the magnetic tension force through the penetration process. Also, in the CT plasmoid injection, the CT is considered to be decelerated by the same process.

4 Discussion

4.1 Effect of Magnetic Reconnection

From figure 10, the difference of the penetration depth between the case 1 and the case 2 is not so different from that between the case 3 and the case 4. However, we can see that the former is a little smaller than the latter. It is because the difference of the CT kinetic energy between the case 1 and the case 2 is a little smaller than that between the case 3 and the case 4 (see figure 11). As shown in the previous section, the decrease of the CT kinetic energy due to the existence of the target magnetic field is caused by the Lorentz force effect which includes effects both of the magnetic pressure force and the magnetic tension force. From these results, it is considered that the Lorentz force effect is relaxed in the CT injection compared with the bare plasmoid injection. As previously indicated, in the CT injection magnetic reconnection takes place, which relaxes the bending of the target magnetic field. Namely, magnetic reconnection would relax the magnetic tension force. In the present simulation, however, the difference of the penetration depth is small as shown previously. It is because the strength of the target magnetic field is small. When it is larger, the relaxation of the magnetic tension force by magnetic reconnection would be more remarkable and contribute to the deep penetration, because the magnetic tension force in such a case becomes more effective.

4.2 Comparison with the experiment

Let us compare the simulation parameters with the experiments. If we take the radius of the injection region L_r to 0.15m, $L_z/2$ becomes 1.2 m, which corresponds to the plasma diameter. For the CT parameters, if it is assumed that the density ρ_{CT} is 1×10^{-5}kg/m^3 (it corresponds to 1×10^{22}/m^3 when it is assumed that the plasma consists of hydrogen) the maximum strength of the magnetic field B_{CT} is 1T, the Alfvén velocity V_A corresponds to 690 km/s. Thus, the injection velocity V_{CT} is 207 km/s. In the target region, the density ρ_{target} corresponds to 1×10^{-7}kg/m^3. The initial pressure P_{com} corresponds to 5 keV in terms of temperature if it is assumed that the plasma consists of hydrogen. Also, the strength of the magnetic field corresponds to 0.1 T for $B_{target} = 0.1$. The resistivity η is fixed to 1×10^{-3} in the normalized unit $\mu_0 L_r V_A$, which corresponds to the $1\times10^{-4}\Omega$ m. Therefore, the strength of the target magnetic field is smaller and the resistivity is larger.

In the simulation, the initial pressure is assumed to be spatially constant. Therefore, the initial pressure in the gun region is the same as that in the target region, which leads to the excessive deceleration of the CT through the compressional heating in the gun region. Since in real experiments the pressure in the gun region is much lower than that in the core plasma, such deceleration would not be caused. However, the pressure in the core plasma is high enough for the injected CT to suffer form the compressional heating, which would cause such a deceleration.

If we assume the Spitzer resistivity, the resistivity in the device region is about $1.0\times10^{-9}\Omega$ m and that in the CT region is about $1.0\times10^{-5}\Omega$ m. Therefore, the resistivity in the present simulation is larger even if the resistivity in the CT region is referred. For smaller resistivity, the injected CT plasmoid would push its way through the target magnetic field predicted by the CS model, which relaxes the magnetic tension force. Also, in the simulation, the target magnetic field is line-tied on the boundary. namely, the magnetic tension force effect is more severe than in the real experiment. These effects cause the excessive deceleration of the CT. In order to examine in more detail, the dependence of the magnetic tension effect on the resistivity, the size of the

target region, and the boundary condition should be investigated.

5 Summary

From our simulation, it can be seen that the process of the CT penetration into the magnetized plasma is much more complicated than what has been analyzed so far by using the CS model. The injected CT suffers from a tilting instability, which grows with the similar time scale as the CT penetration. The instability is accompanied by magnetic reconnection between the CT magnetic field and the target magnetic field. Because this process proceeds successively, the magnetic configuration of the CT is disrupted, which leads to supply of the CT high density plasma into the target plasma region. Also, it can be seen that the penetration depth of the CT high density plasma is shorter than that estimated from the CS model. The injected CT slows down even when the target magnetic field is null, because the CT kinetic energy is decreased by the compressional heating. When the target magnetic field exists, the CT is more decelerated by the Lorentz force effect through the compressibility of plasma, by which the CT kinetic energy is converted to the magnetic energy of the target magnetic field. By comparing the CT injection with the bare plasmoid injection, the Lorentz force effect in the CT injection is considered to be relaxed by magnetic reconnection.

In the present simulation the strength of the target magnetic field is small. To investigate the CT dynamics as well as the penetration depth in more detail, the dependence of the target magnetic field should be considered.

Acknowledgments

We acknowledge Dr. K. Kusano, for useful discussions. We thank Prof. M.J. Gouge, Prof. R. Raman, Prof. O. Motojima, Dr. H. Yamada, Dr. J. Miyazawa, Prof. T. Uyama, Dr. M. Nagata, and Dr. N. Fukumoto for fruitful suggestions. This research is supported by a Grant-in-Aid from the Ministry of Education, Science, Sports and Culture in Japan. One of the authors (Y.S.) was also supported by the Japan Society of the Promotion of Science.

References

[1] BROWN, M.R., BELLAN, P.M., Nucl. Fusion **32** (1992) 1125.

[2] RAMAN, R., *et al.*, Phys. Rev. Lett. **73** (1994) 3101.

[3] RAMAN, R., *et al.*, Nucl. Fusion **37** (1997) 967.

[4] GOUGE, M.J., *et al.*, in Proceedings of the Sixteenth IAEA Fusion Energy Conference, Montréal, Canada, October 1996.

[5] FUKUMOTO, N., *et al.*, Bull. Amer. Phys. Soc. **42** (1997) 1961.

[6] OGAWA, T., *et al.*, 17th IAEA Fusion Energy Conference, Yokohama, IAEA-F1-CN-69, 1998

[7] PARKS, P.B., Phys. Rev. Lett. **61** (1988) 1364.

[8] PERKINS, L.J., HO, S.K., HAMMER, J.H., Nucl. Fusion **28** (1988) 1365.

[9] NEWCOMB, W.A., Phys. Fluids B **3** (1991) 1818.

[10] SUZUKI, Y., *et al.*, in Proceedings of the Joint Conference of 11th International Stellarator Conference & 8th International Toki Conference on Plasma Physics and Controlled Nuclear Fusion, ed. Y.Ueda **1** 518 (1998).

[11] SUZUKI, Y., WATANABE, T-H., SATO, T., HAYASHI, T., to be published in Proceedings of the GA of APFA and APPTC (1999).

[12] FINN, J.M., MANHEIMER, W.M., Phys. Fluids **24** (1981) 1336.

[13] SATO, T., HAYASHI, T., Phys. Rev. Lett. **50** (1983) 38.

[14] HAYASHI, T., SATO, T., Phys. Fluids. **28** (1985) 12.

[15] KUSANO, K., SUZUKI, Y., SATO, T., NISHIKAWA, K., Phys. Fluids B **5** (1993) 357.

Figure Captions

Fig.1: Schematic diagram of the simulation region. The CT magnetic field and the target magnetic field are directed as shown here.

Fig.2: The spatial structure of the magnetic flux (contours) and the plasma density (colors) viewed from $\theta = 0$ at $t = 0, 20, 40$, and $60\tau_A$ in the case 1.

Fig.3: The spatial structure of magnetic field lines and the high density plasma viewed from $\theta = 0$ at $t = 0, 20, 40$, and $60\tau_A$ in the case 2.

Fig.4: The time evolution of contours for the plasma density viewed from $\theta = 0$ at $t = 0, 20, 40$, and $60\tau_A$ in the case 2.

Fig.5: The magnetic structure and the high density plasma at $t = 20\tau_A$ viewed from various directions. Yellow lines are the CT magnetic field, blue lines are the target magnetic field which does not reconnect with the CT magnetic field, and green lines are the magnetic field reconnected between the CT magnetic field and the target magnetic field.

Fig.6: The time evolution of penetration depths in the simulation and in the CS model. Penetration depths with $B_{\rm target} = 0$ and with $B_{\rm target} = 0.1$ are respectively plotted by solid lines and broken lines both in the simulation and the CS model.

Fig.7: The time evolution of the CT kinetic energy, which is defined by the kinetic energy integrated in the CT region ($E_{\rm k}^{\rm CT} \equiv \int_{\rho>\rho_c} \frac{1}{2}\rho V^2 dv$). The solid line and the broken line correspond to the case 1 and the case 2, respectively. The time evolution of the CS kinetic energy estimated from the CS model is also plotted.

Fig.8: The schematic diagram of the energy conversion between the kinetic energy, the magnetic energy, and the thermal energy which are divided into the CT region and the background region.

Fig.9: The time history of energy conversion rates: the viscous heating $\dot{\varepsilon}^{\rm v}_{\rm k\to t}$ the compressional heating $\dot{\varepsilon}^{\rm c}_{\rm k\to t}$ the Lorentz force effect $\dot{\varepsilon}_{\rm k\to m}$, and the outflow to the background region $\dot{\varepsilon}_{\rm k}^{\rm CT\to back}$. These rates are integrated in the CT region ($\rho > \rho_c$).

Fig.10: The difference of the penetration depth between the case 1 and the case 2 (solid line) and that estimated from the CS model (broken line). The difference of it between the case 3 and the case 4 is also plotted by a broken line. Since, the bare plasmoid reaches the opposite wall by $t = 40\tau_A$, after that, it is eliminated.

Fig.11: The difference of the CT kinetic energy between the case 1 and the case 2 (solid line) and that of the CS kinetic energy between cases with $B_{\rm target} = 0$ and with $B_{\rm target} = 0.1$ (broken line). That between the case 3 and the case 4 is also plotted by a broken line. The reason why it in the bare plasmoid injection becomes smaller at $t = 38\tau_A$ is the effect of the opposite wall.

Fig.12: The difference of energy conversion rates between the case 1 and the case 2. These are integrated in the CT region and subtracted those in the case 1 from in the case 2, $\delta\dot{\varepsilon} = \int_{\rho>\rho_c} \dot{\varepsilon} dv|_{\rm case2} - \int_{\rho>\rho_c} \dot{\varepsilon} dv|_{\rm case1}$.

Fig.13: The resultant energy difference and the converted energy between $t = 7\tau_A$ and $t = 40\tau_A$ subtracted those in the case 1 from in the case 2.

Fig.14: The spatial structure of the plasma density (colors) viewed from $\theta = 0$ at $t = 0, 20, 40$, and $60\tau_A$ in the case 3.

Fig.15: The spatial structure of magnetic field lines and the high density plasma viewed from $\theta = 0$ at $t = 0, 20, 40$, and $60\tau_A$ in the case 4.

Fig.16: The time evolution of energy conversion rates due to the Lorentz force effect of the target magnetic field in the case 4. These rates are integrated in the background region ($\rho \leq \rho_c$).

	CT			target		common
case	V_{CT}	ρ_{CT}	B_{CT}	ρ_{target}	B_{target}	P_{com}
1	0.3	10	1	0.1	0	0.1
2	0.3	10	1	0.1	0.1	0.1
3	0.3	10	0	0.1	0	0.1
4	0.3	10	0	0.1	0.1	0.1

Table 1: Several parameters in four different simulation runs.

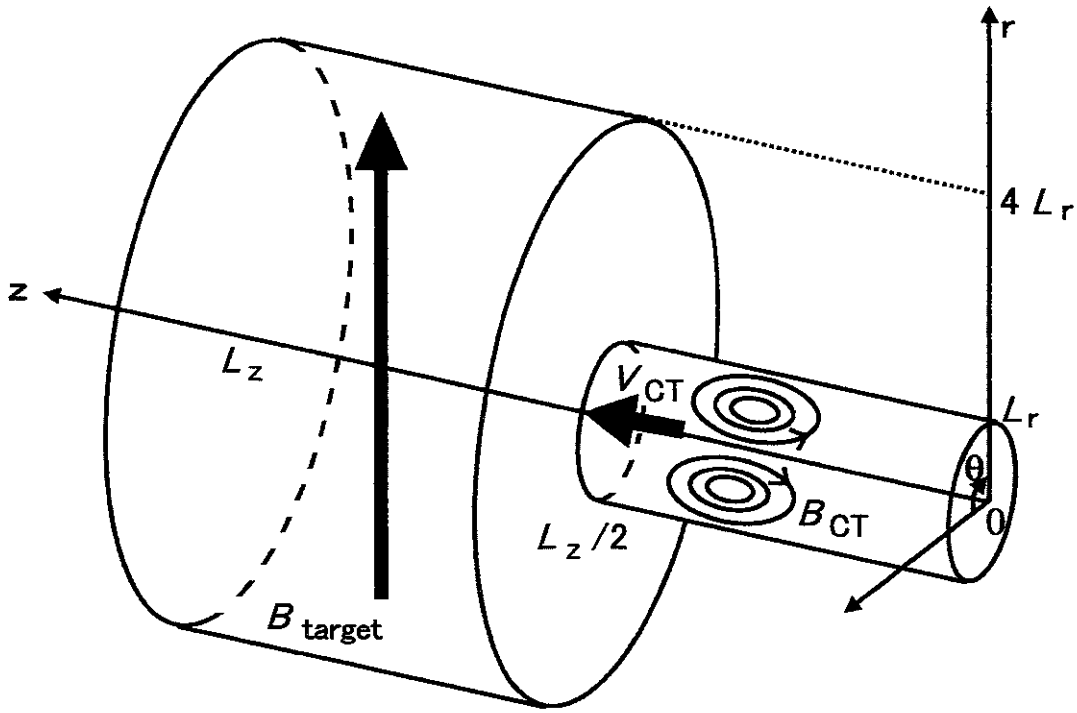

Fig.1

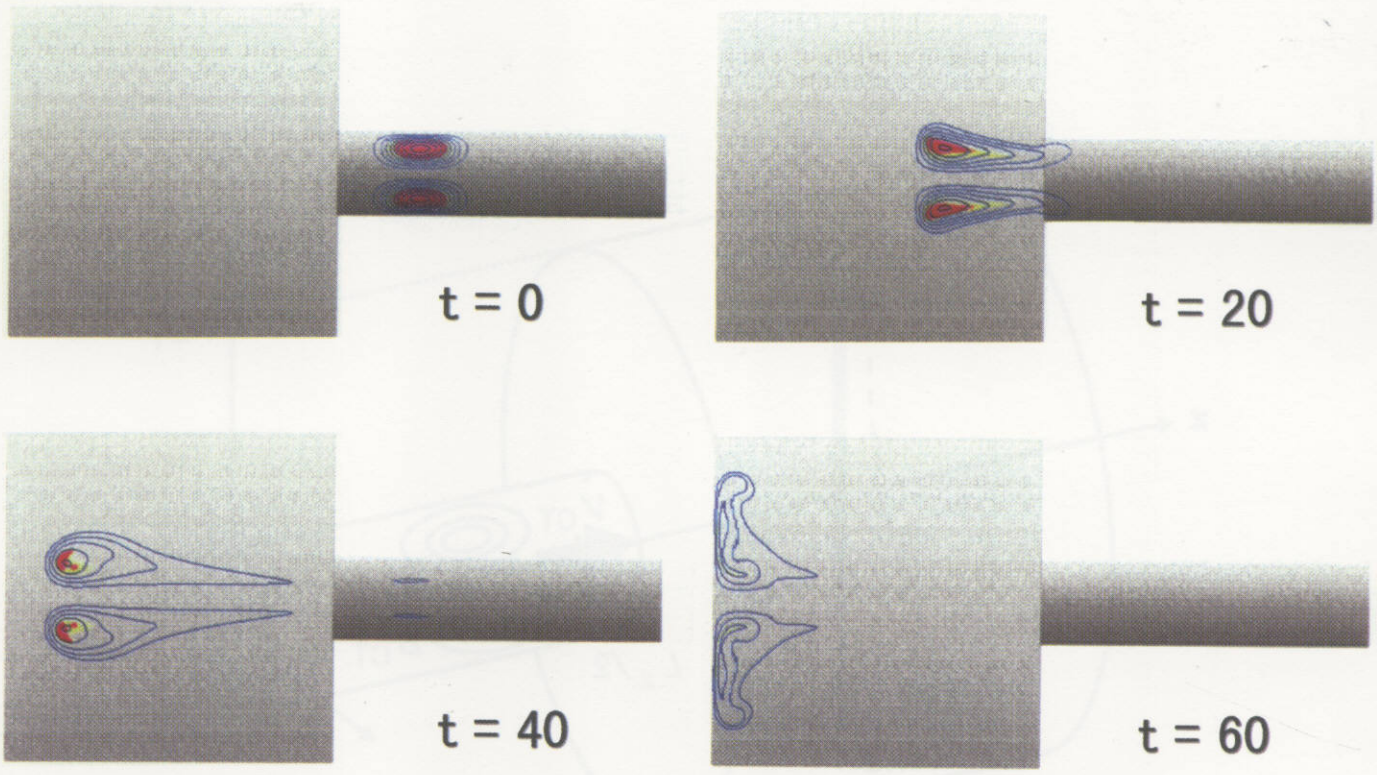

Fig.2

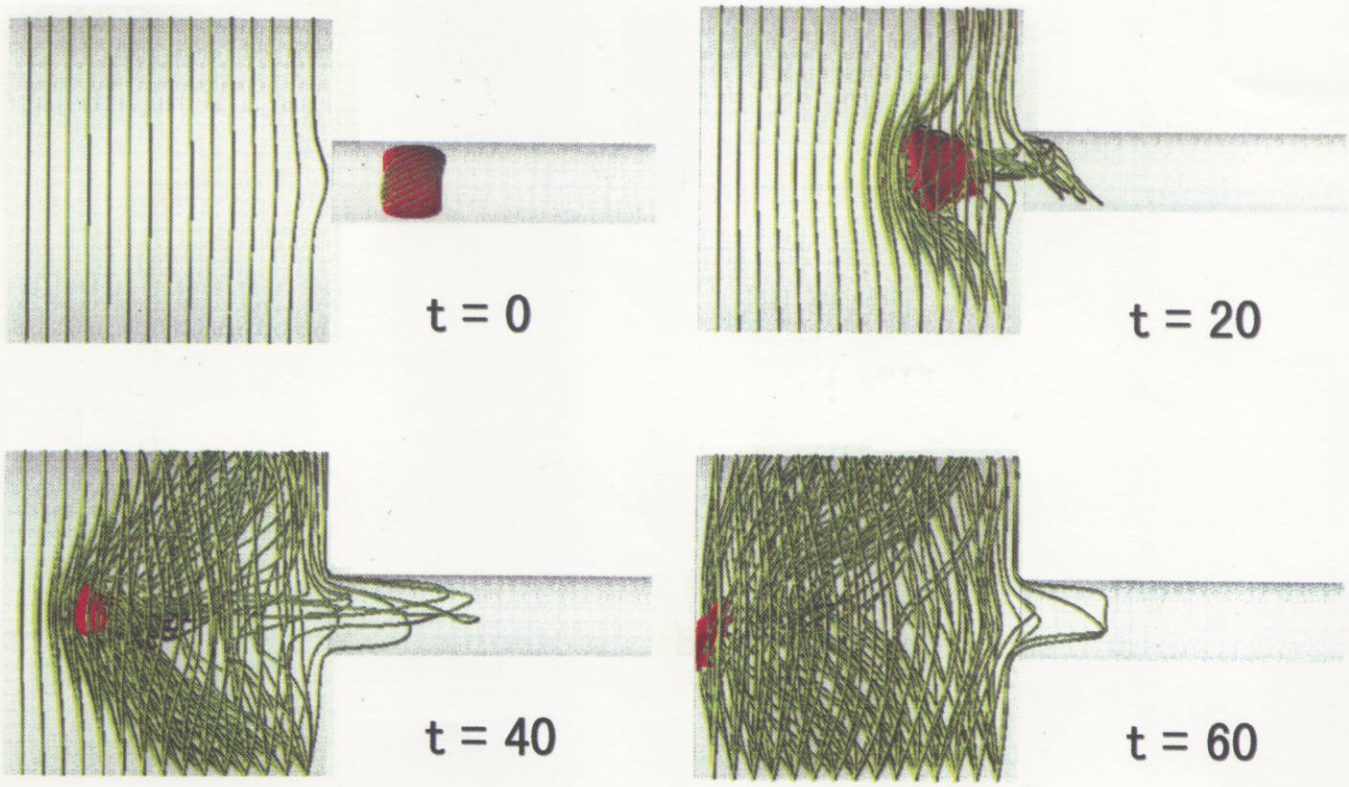

Fig.3

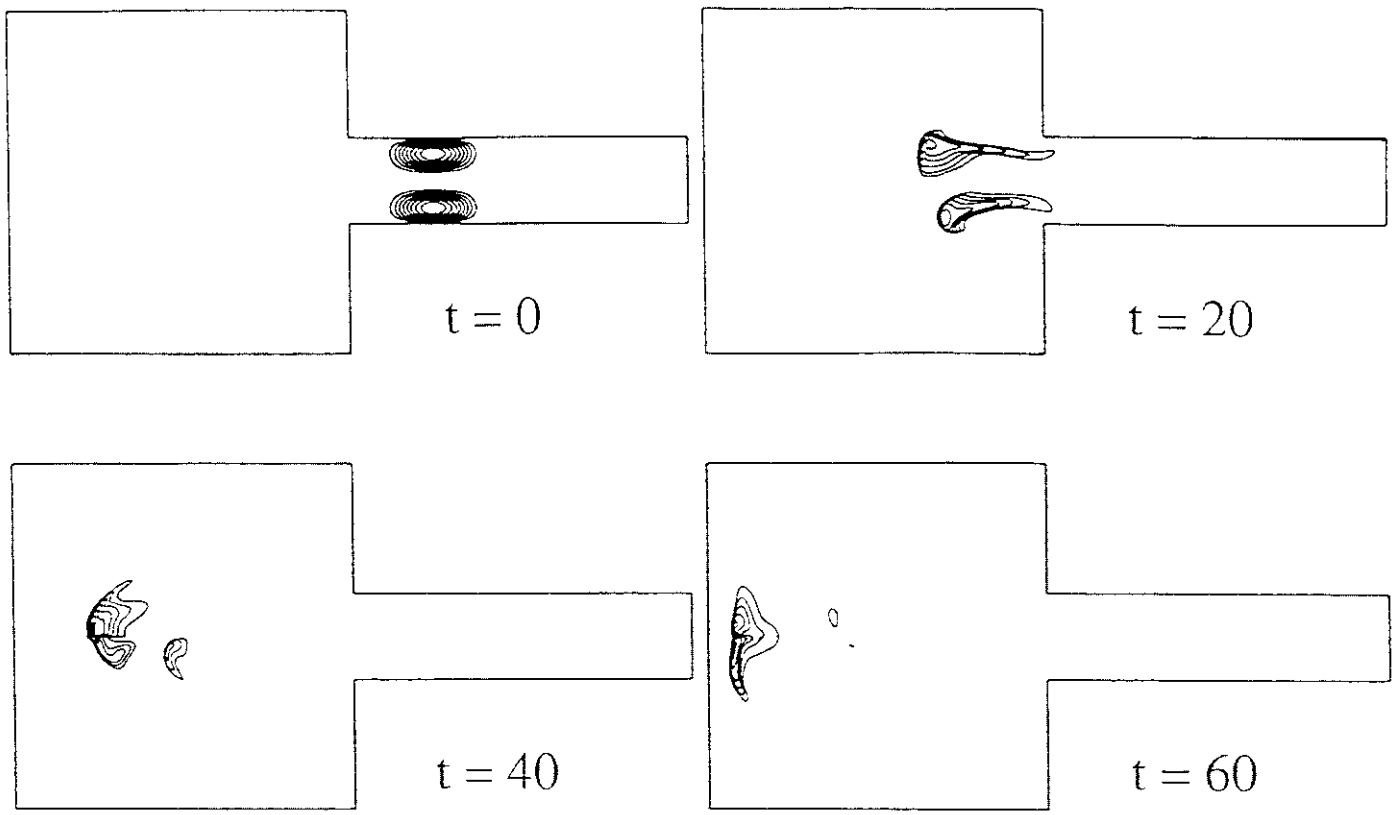

Fig.4

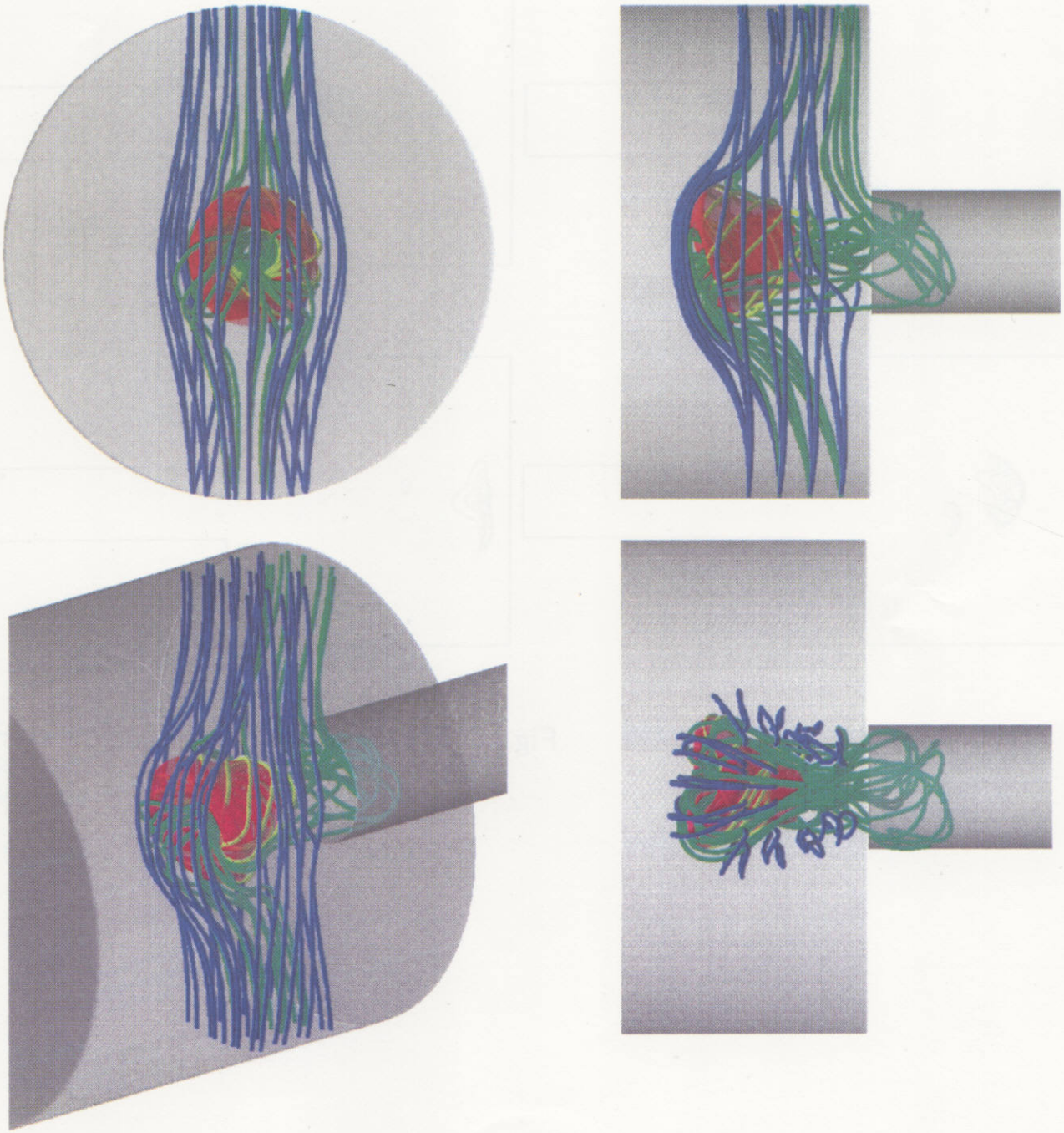

Fig.5

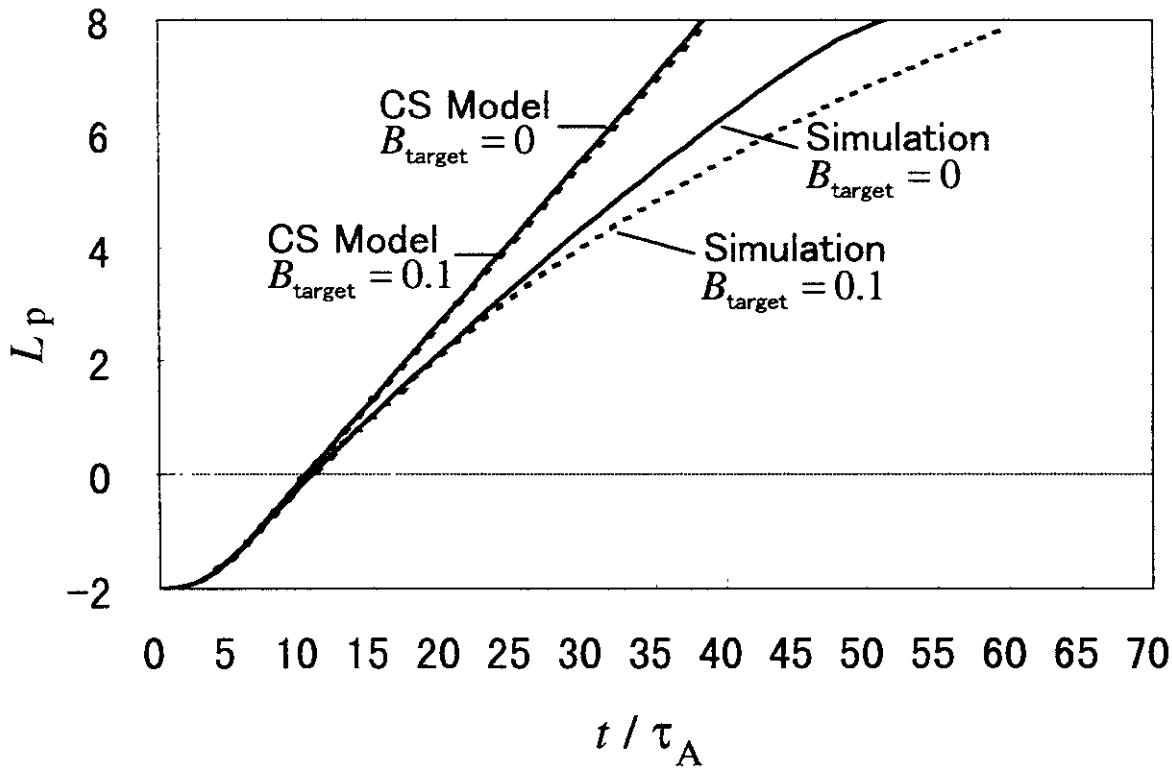
8
6
4
2
0
−2
L_p
CS Model
$B_{target} = 0$
CS Model
$B_{target} = 0.1$
Simulation
$B_{target} = 0$
Simulation
$B_{target} = 0.1$
0 5 10 15 20 25 30 35 40 45 50 55 60 65 70
t / τ_A

Fig.6

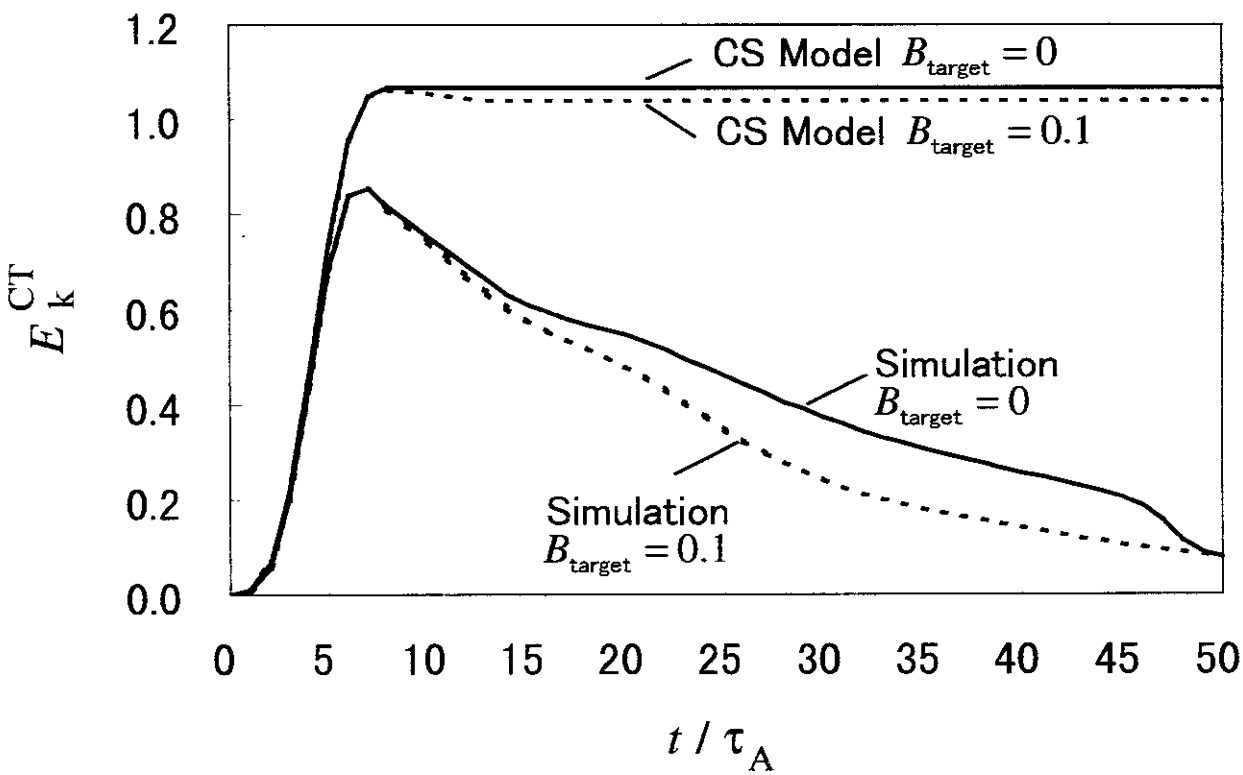
1.2
1.0
0.8
0.6
0.4
0.2
0.0
E_k^{CT}
CS Model $B_{target} = 0$
CS Model $B_{target} = 0.1$
Simulation
$B_{target} = 0$
Simulation
$B_{target} = 0.1$
0 5 10 15 20 25 30 35 40 45 50
t / τ_A

Fig.7

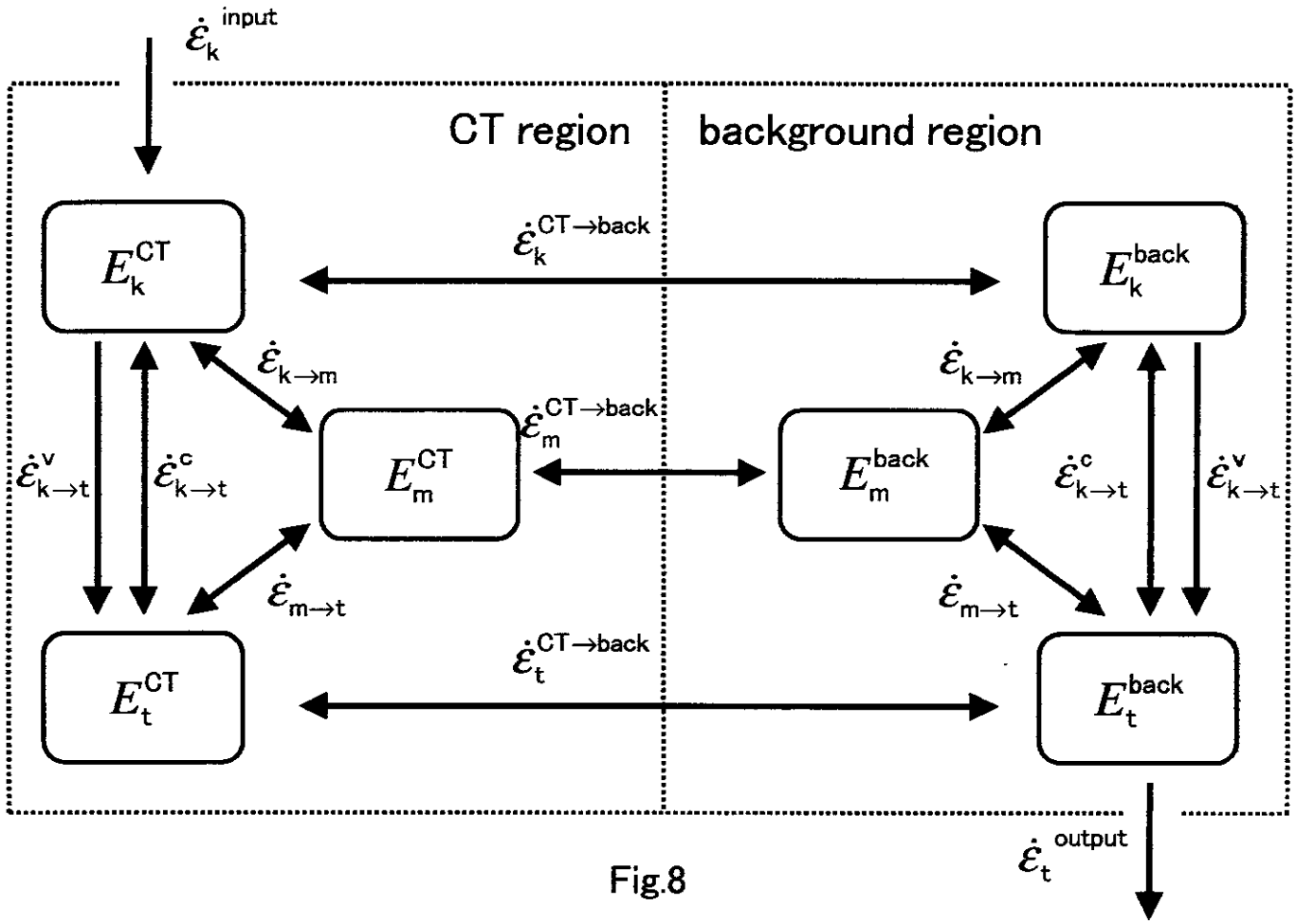
$\dot{\varepsilon}_k^{input}$
CT region
background region
E_k^{CT}
$\dot{\varepsilon}_k^{CT\to back}$
E_k^{back}
$\dot{\varepsilon}_{k\to m}$
$\dot{\varepsilon}_{k\to m}$
$\dot{\varepsilon}_m^{CT\to back}$
$\dot{\varepsilon}_{k\to t}^{v}$
$\dot{\varepsilon}_{k\to t}^{c}$
E_m^{CT}
E_m^{back}
$\dot{\varepsilon}_{k\to t}^{c}$
$\dot{\varepsilon}_{k\to t}^{v}$
$\dot{\varepsilon}_{m\to t}$
$\dot{\varepsilon}_{m\to t}$
$\dot{\varepsilon}_t^{CT\to back}$
E_t^{CT}
E_t^{back}
$\dot{\varepsilon}_t^{output}$

Fig.8

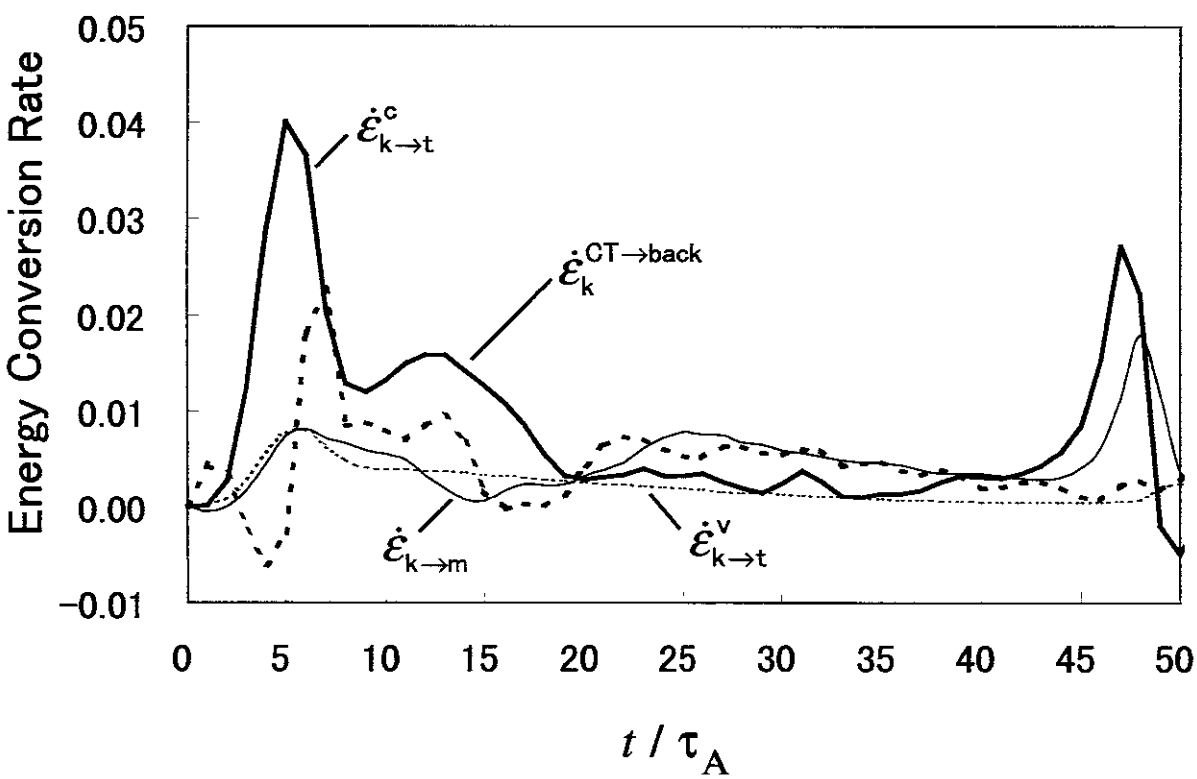
Energy Conversion Rate
0.05
0.04
0.03
0.02
0.01
0.00
−0.01
0
5
10
15
20
25
30
35
40
45
50
t / τ_A
$\dot{\varepsilon}_{k\to t}^{c}$
$\dot{\varepsilon}_k^{CT\to back}$
$\dot{\varepsilon}_{k\to m}$
$\dot{\varepsilon}_{k\to t}^{v}$

Fig.9

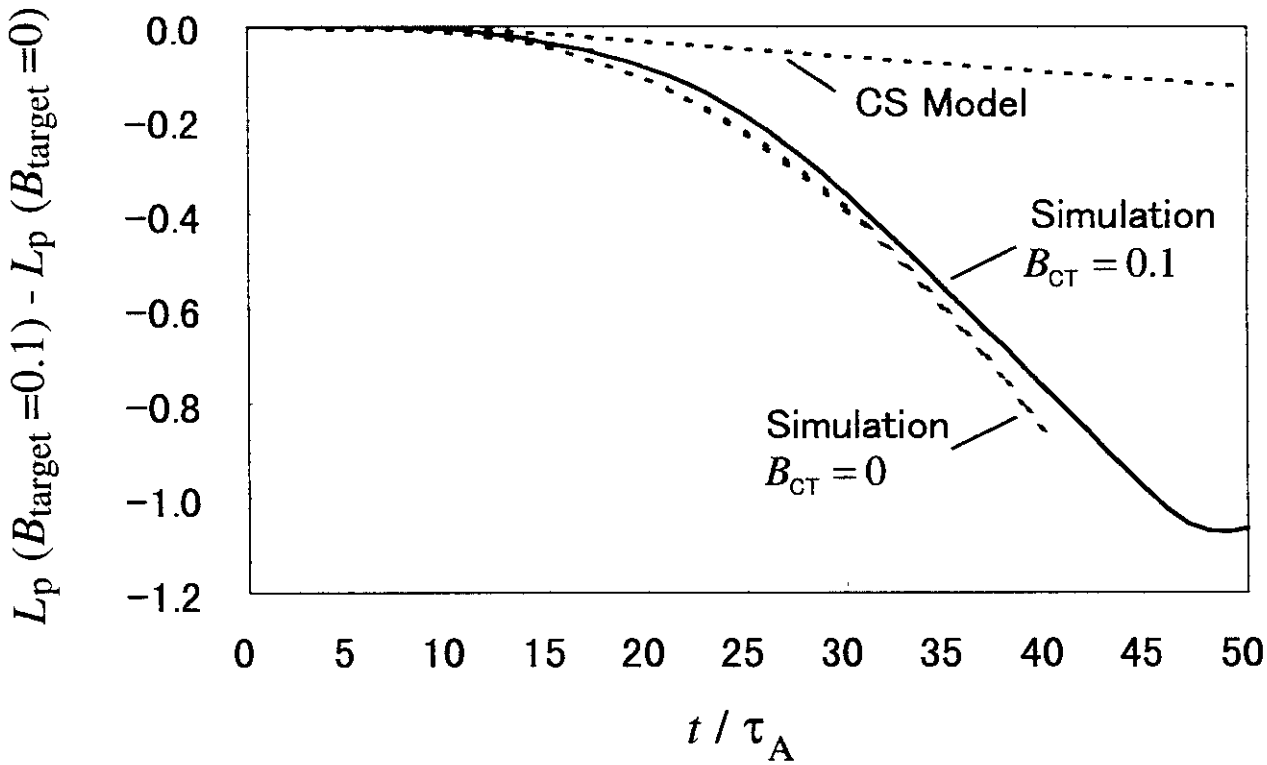
0.0
−0.2
−0.4
−0.6
−0.8
−1.0
−1.2
L_p (B_{target} =0.1) - L_p (B_{target} =0)
CS Model
Simulation
B_{CT} = 0.1
Simulation
B_{CT} = 0
0
5
10
15
20
25
30
35
40
45
50
t / τ_A

Fig.10

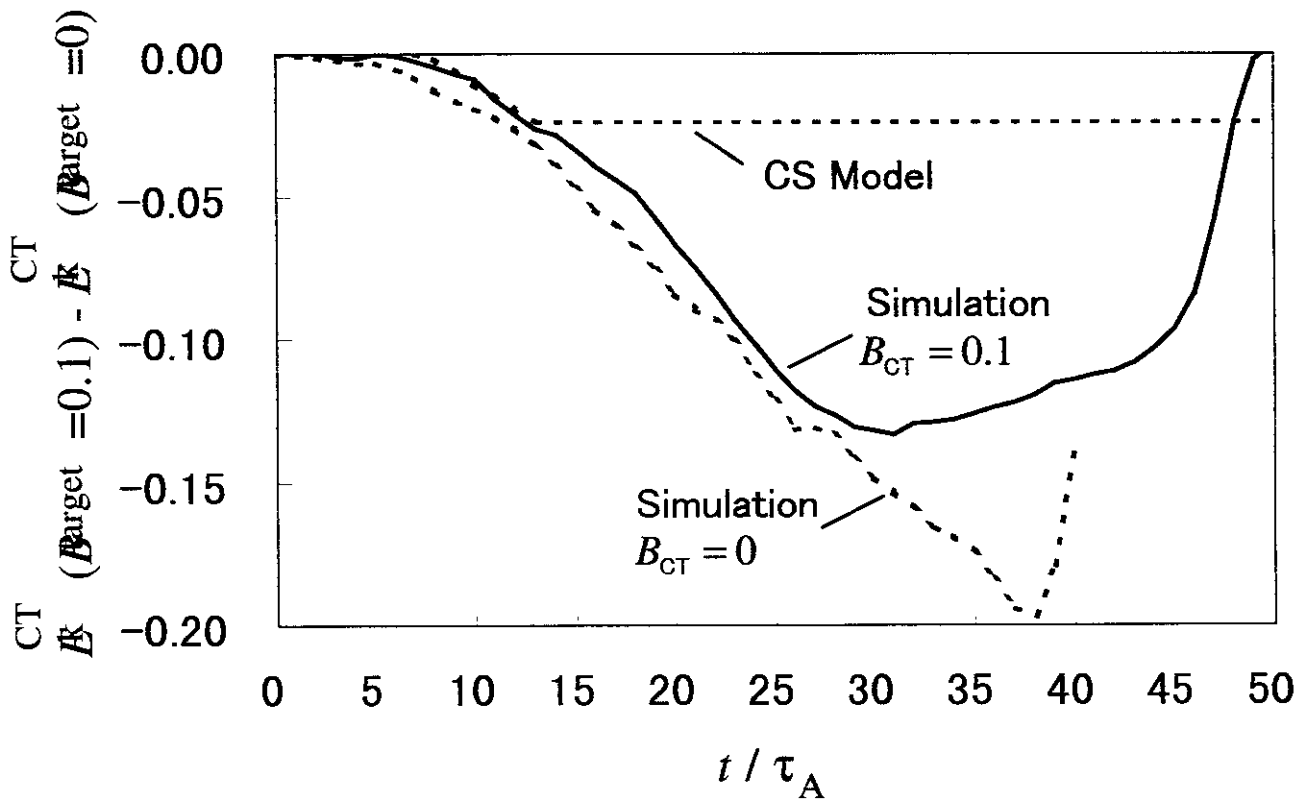
0.00
−0.05
−0.10
−0.15
−0.20
CS Model
Simulation
B_{CT} = 0.1
Simulation
B_{CT} = 0
0
5
10
15
20
25
30
35
40
45
50
t / τ_A

Fig.11

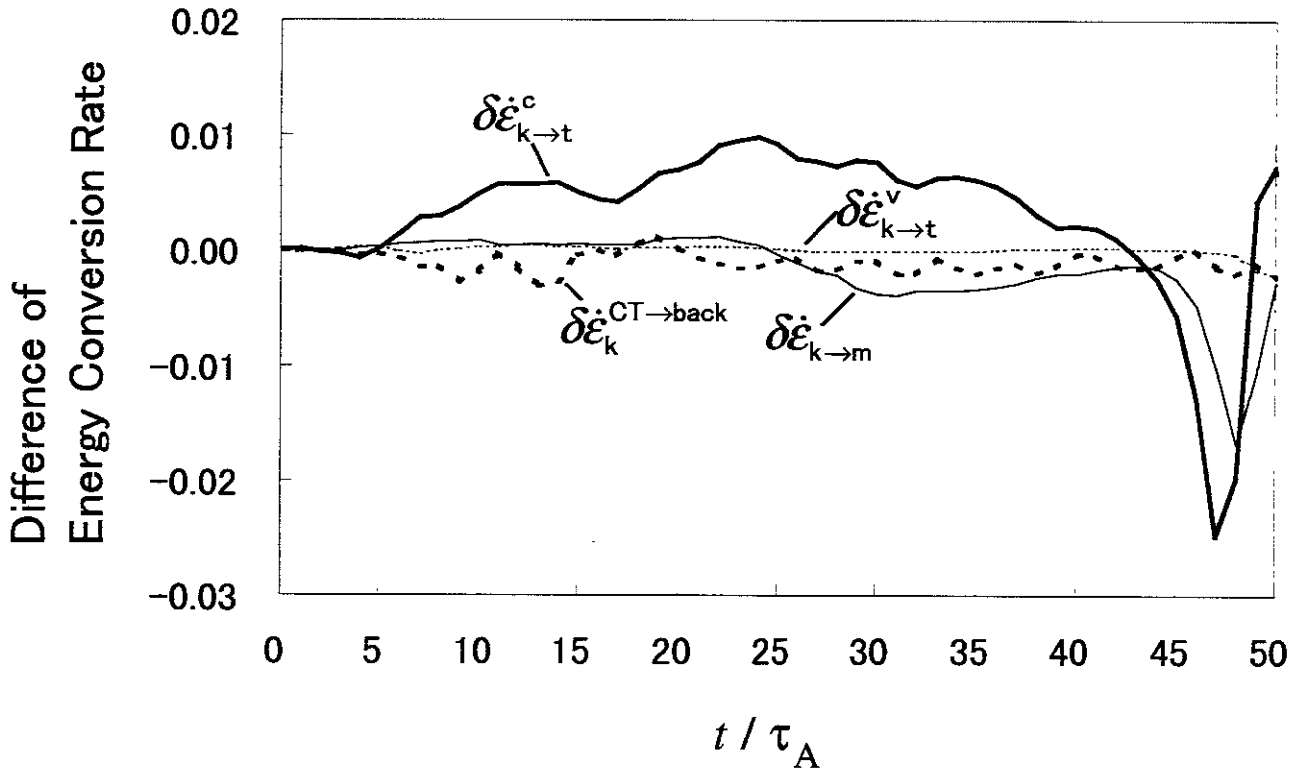
Difference of Energy Conversion Rate
0.02
0.01
0.00
−0.01
−0.02
−0.03
0
5
10
15
20
25
30
35
40
45
50
t / τ_A
$\delta\dot{\varepsilon}^{c}_{k\to t}$
$\delta\dot{\varepsilon}^{v}_{k\to t}$
$\delta\dot{\varepsilon}^{CT\to back}_{k}$
$\delta\dot{\varepsilon}_{k\to m}$

Fig.12

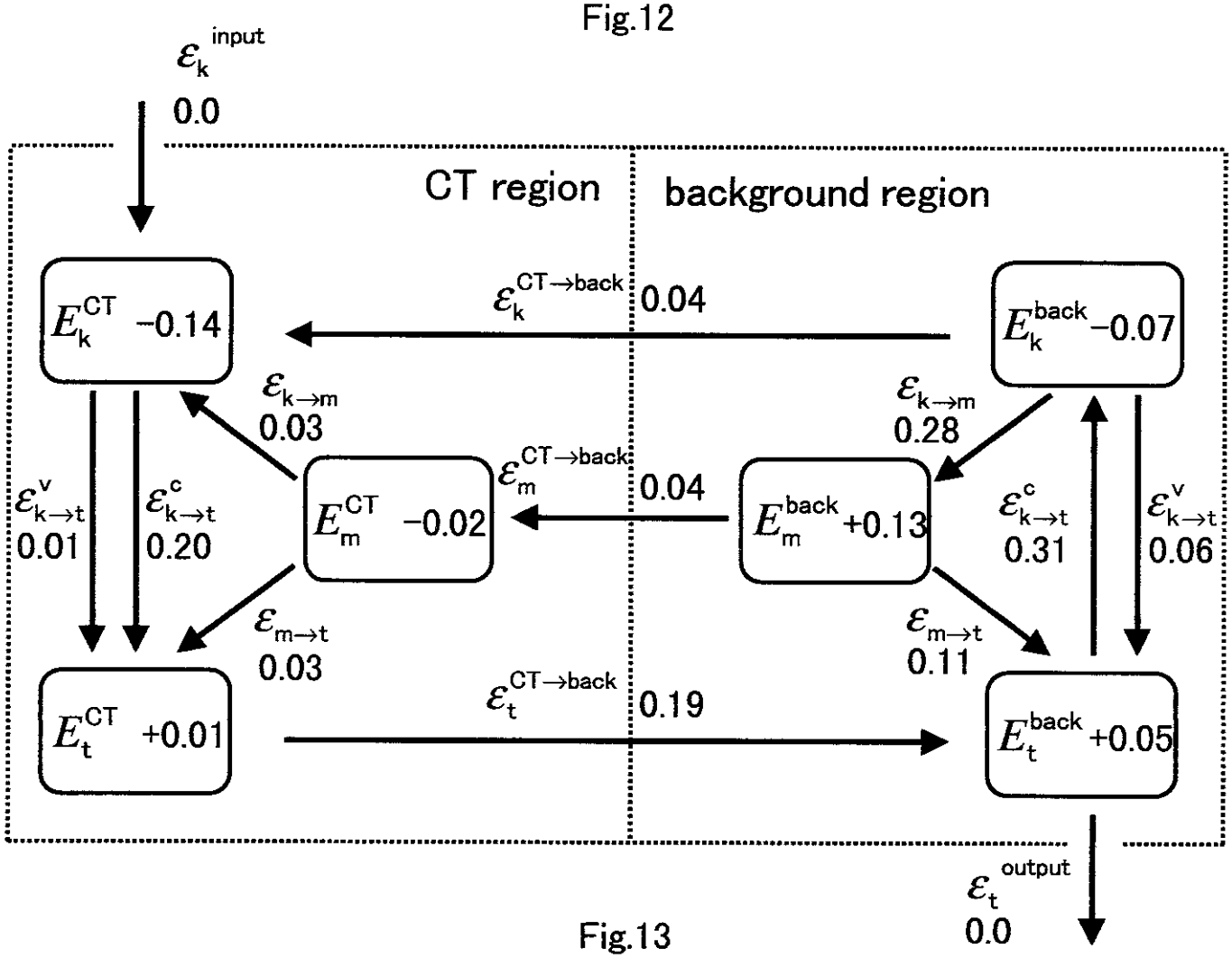
ε_k^{input}
0.0
CT region
background region
E_k^{CT} −0.14
E_m^{CT} −0.02
E_t^{CT} +0.01
E_k^{back} −0.07
E_m^{back} +0.13
E_t^{back} +0.05
$\varepsilon_k^{CT\to back}$ 0.04
$\varepsilon_{k\to m}$ 0.03
$\varepsilon_{k\to m}$ 0.28
$\varepsilon_m^{CT\to back}$ 0.04
$\varepsilon^{v}_{k\to t}$ 0.01
$\varepsilon^{c}_{k\to t}$ 0.20
$\varepsilon^{c}_{k\to t}$ 0.31
$\varepsilon^{v}_{k\to t}$ 0.06
$\varepsilon_{m\to t}$ 0.03
$\varepsilon_{m\to t}$ 0.11
$\varepsilon_t^{CT\to back}$ 0.19
ε_t^{output}
0.0

Fig.13

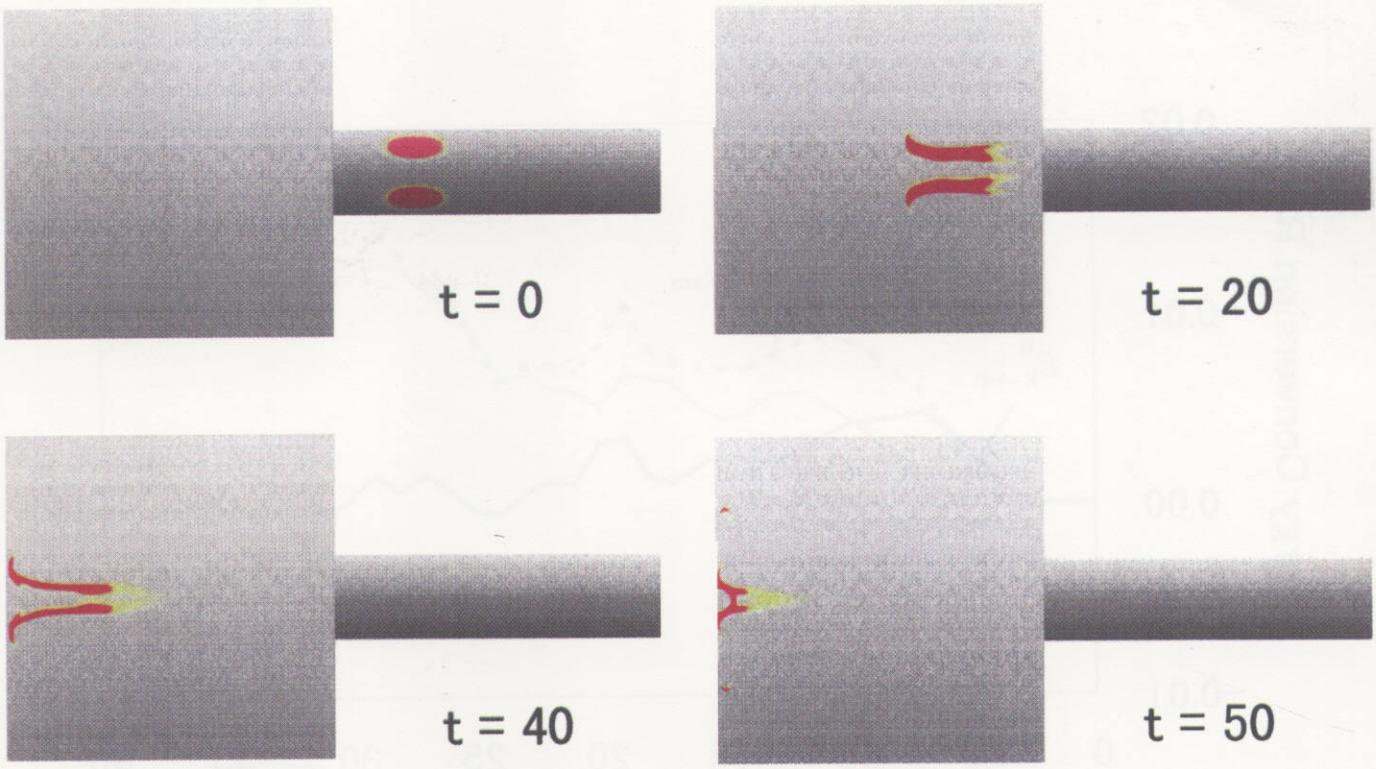

Fig.14

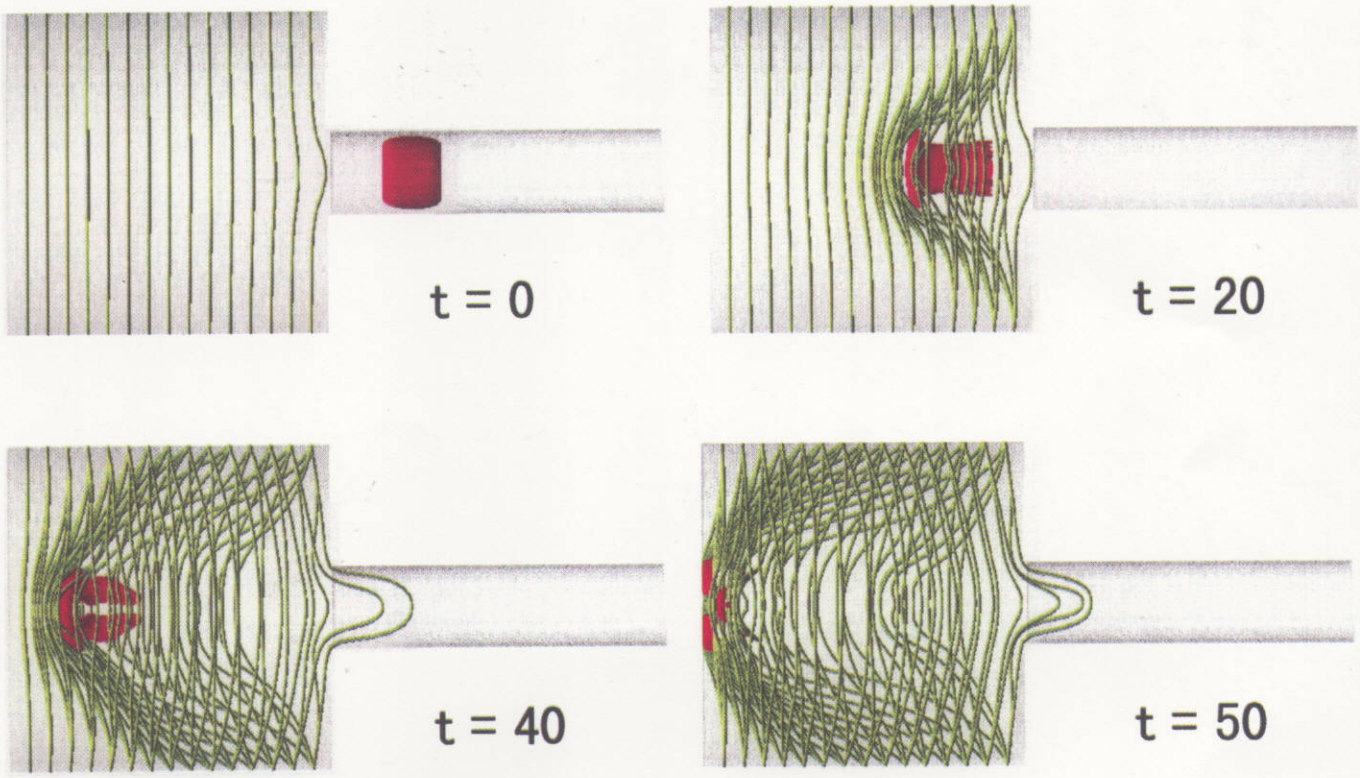

Fig.15

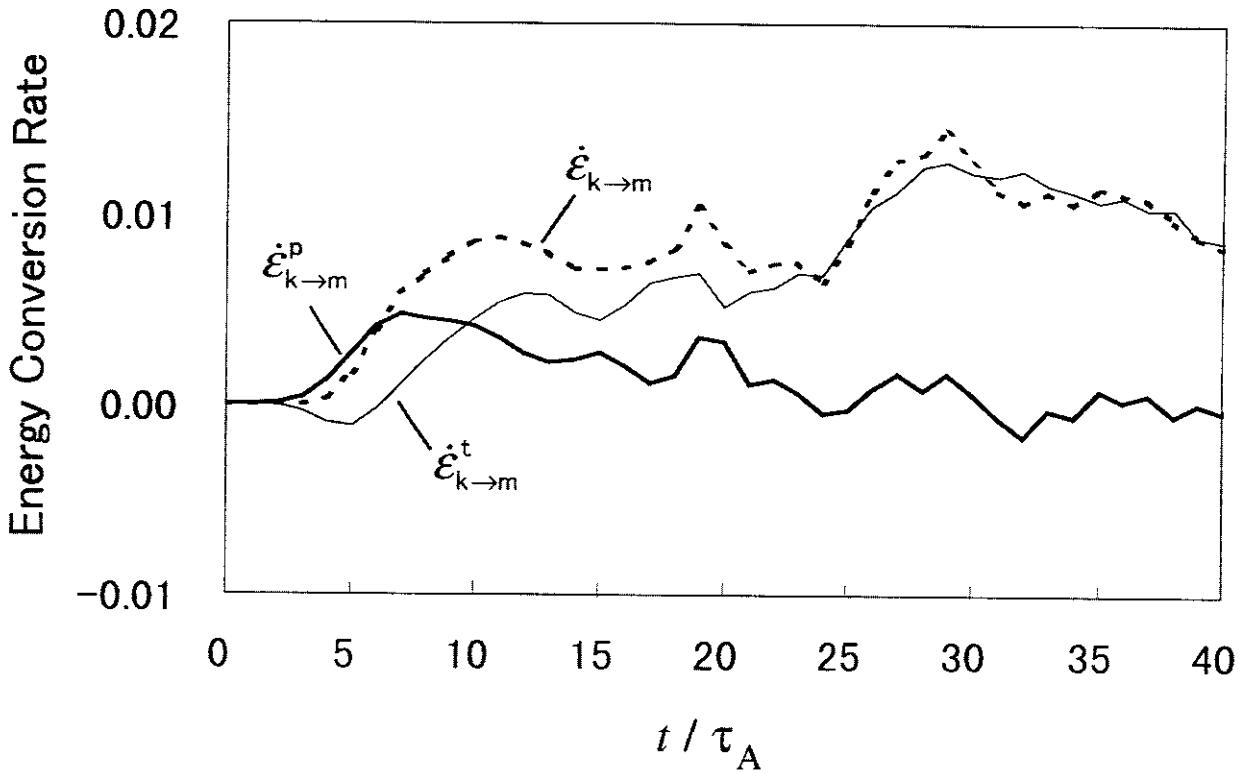
0.02
0.01
0.00
−0.01
Energy Conversion Rate
$\dot{\varepsilon}_{k\to m}$
$\dot{\varepsilon}^{p}_{k\to m}$
$\dot{\varepsilon}^{t}_{k\to m}$
0
5
10
15
20
25
30
35
40
t / τ_A

Fig.16

Recent Issues of NIFS Series

NIFS-532 J Uramoto,
Pair Creations of Negative and Positive Pionlike (Muonlike) Particle or K Mesonlike (Muonlike) Particle in H2 or D2 Gas Discharge in Magnetic Field, Dec 1997

NIFS-533 S Kawata, C Boonmee, T. Teramoto, L Drska, J Limpouch, R Liska, M Sinor,
Computer-Assisted Particle-in-Cell Code Development, Dec. 1997

NIFS-534 Y. Matsukawa, T. Suda, S. Ohnuki and C. Namba,
Microstructure and Mechanical Property of Neutron Irradiated TiNi Shape Memory Alloy, Jan 1998

NIFS-535 A Fujisawa, H Iguchi, H Idei, S Kubo, K. Matsuoka, S. Okamura, K. Tanaka, T Minami, S. Ohdachi, S Morita, H. Zushi, S. Lee, M. Osakabe, R. Akiyama, Y Yoshimura, K. Toi, H. Sanuki, K. Itoh, A Shimizu, S. Takagi, A Ejiri, C Takahashi, M Kojima, S. Hidekuma, K. Ida, S. Nishimura, N. Inoue, R Sakamoto, S -I. Itoh, Y. Hamada, M. Fujiwara,
Discovery of Electric Pulsation in a Toroidal Helical Plasma; Jan. 1998

NIFS-536 Lj.R. Hadzievski, M.M. Skoric, M Kono and T Sato,
Simulation of Weak and Strong Langmuir Collapse Regimes; Jan. 1998

NIFS-537 H Sugama, W. Horton,
Nonlinear Electromagnetic Gyrokinetic Equation for Plasmas with Large Mean Flows, Feb 1998

NIFS-538 H. Iguchi, T P. Crowley, A. Fujisawa, S Lee, K Tanaka, T Minami, S Nishimura, K. Ida, R. Akiyama, Y. Hamada, H., Idei. M. Isobe, M. Kojima, S Kubo, S Morita, S Ohdachi, S. Okamura, M Osakabe, K. Matsuoka, C Takahashi and K Toi,
Space Potential Fluctuations during MHD Activities in the Compact Helical System (CHS); Feb 1998

NIFS-539 Takashi Yabe and Yan Zhang,
Effect of Ambient Gas on Three-Dimensional Breakup in Coronet Formation Process, Feb. 1998

NIFS-540 H. Nakamura, K. Ikeda and S. Yamaguchi,
Transport Coefficients of InSb in a Strong Magnetic Field, Feb 1998

NIFS-541 J. Uramoto,
Development of ν_μ Beam Detector and Large Area ν_μ Beam Source by H_2 Gas Discharge (I); Mar. 1998

NIFS-542 J. Uramoto,
Development of bar{ν}$_\mu$ Beam Detector and Large Area bar{ν}$_\mu$ Beam Source by H_2 Gas Discharge (II); Mar 1998

NIFS-543 J. Uramoto,
Some Problems inside a Mass Analyzer for Pions Extracted from a H_2 Gas Discharge; Mar. 1998

NIFS-544 J. Uramoto,
Simplified ν_μ bar{ν}$_\mu$ Beam Detector and ν_μ bar{ν}$_\mu$ Beam Source by Interaction between an Electron Bunch and a Positive Ion Bunch; Mar. 1998

NIFS-545 J Uramoto,
Various Neutrino Beams Generated by D_2 Gas Discharge; Mar.1998

NIFS-546 R. Kanno, N Nakajima, T. Hayashi and M. Okamoto,
Computational Study of Three Dimensional Equilibria with the Bootstrap Current; Mar. 1998

NIFS-547 R. Kanno, N. Nakajima and M Okamoto,
Electron Heat Transport in a Self-Similar Structure of Magnetic Islands; Apr. 1998

NIFS-548 J.E Rice,
Simulated Impurity Transport in LHD from MIST; May 1998

NIFS-549 M.M Skoric, T. Sato, A.M Maluckov and M.S Jovanovic,
On Kinetic Complexity in a Three-Wave Interaction; June 1998

NIFS-550 S. Goto and S. Kida,
Passive Saclar Spectrum in Isotropic Turbulence: Prediction by the Lagrangian Direct-interaction Approximation; June 1998

NIFS-551 T. Kuroda, H. Sugama, R. Kanno, M. Okamoto and W. Horton,
Initial Value Problem of the Toroidal Ion Temperature Gradient Mode ; June 1998

NIFS-552 T. Mutoh, R. Kumazawa, T. Seki, F. Simpo, G. Nomura, T. Ido and T. Watari,
Steady State Tests of High Voltage Ceramic Feedthoughs and Co-Axial Transmission Line of ICRF Heating System for the Large Helical Device ; June 1998

NIFS-553 N. Noda, K. Tsuzuki, A. Sagara, N. Inoue, T. Muroga,
oronaization in Future Devices -Protecting Layer against Tritium and Energetic Neutrals-: July 1998

NIFS-554 S. Murakami and H. Saleem,
Electromagnetic Effects on Rippling Instability and Tokamak Edge Fluctuations; July 1998

NIFS-555 H. Nakamura , K. Ikeda and S. Yamaguchi,
Physical Model of Nernst Element; Aug. 1998

NIFS-556 H. Okumura, S. Yamaguchi, H. Nakamura, K. Ikeda and K. Sawada,
Numerical Computation of Thermoelectric and Thermomagnetic Effects; Aug. 1998

NIFS-557 Y. Takeiri, M. Osakabe, K. Tsumori, Y Oka, O. Kaneko, E. Asano, T. Kawamoto, R. Akiyama and M Tanaka,
Development of a High-Current Hydrogen-Negative Ion Source for LHD-NBI System, Aug.1998

NIFS-558 M. Tanaka, A. Yu Grosberg and T. Tanaka,
Molecular Dynamics of Structure Organization of Polyampholytes, Sep. 1998

NIFS-559 R. Horiuchi, K. Nishimura and T. Watanabe,
Kinetic Stabilization of Tilt Disruption in Field-Reversed Configurations; Sep. 1998
(IAEA-CN-69/THP1/11)

NIFS-560 S. Sudo, K. Kholopenkov, K. Matsuoka, S. Okamura, C. Takahashi, R. Akiyama, A. Fujisawa, K. Ida, H. Idei, H. Iguchi, M. Isobe, S. Kado, K. Kondo, S. Kubo, H. Kuramoto, T. Minami, S. Morita, S. Nishimura, M. Osakabe, M. Sasao, B. Peterson, K. Tanaka, K. Toi and Y. Yoshimura,
Particle Transport Study with Tracer-Encapsulated Solid Pellet Injection; Oct. 1998
(IAEA-CN-69/EXP1/18)

NIFS-561 A. Fujisawa, H. Iguchi, S. Lee, K. Tanaka, T. Minami, Y. Yoshimura, M. Osakabe, K. Matsuoka, S. Okamura, H. Idei, S. Kubo, S. Ohdachi, S. Morita, R. Akiyama, K. Toi, H. Sanuki, K. Itoh, K. Ida, A. Shimizu, S. Takagi, C. Takahashi, M. Kojima, S. Hidekuma, S. Nishimura, M. Isobe, A. Ejiri, N. Inoue, R. Sakamoto, Y. Hamada and M. Fujiwara,
Dynamic Behavior Associated with Electric Field Transitions in CHS Heliotron/Torsatron, Oct. 1998
(IAEA-CN-69/EX5/1)

NIFS-562 S. Yoshikawa,
Next Generation Toroidal Devices; Oct. 1998

NIFS-563 Y. Todo and T. Sato,
Kinetic-Magnetohydrodynamic Simulation Study of Fast Ions and Toroidal Alfvén Eigenmodes; Oct. 1998
(IAEA-CN-69/THP2/22)

NIFS-564 T. Watari, T. Shimozuma, Y. Takeiri, R. Kumazawa, T. Mutoh, M. Sato, O. Kaneko, K. Ohkubo, S. Kubo, H. Idei, Y. Oka, M. Osakabe, T. Seki, K. Tsumori, Y. Yoshimura, R. Akiyama, T. Kawamoto, S. Kobayashi, F. Shimpo, Y. Takita, E. Asano, S. Itoh, G. Nomura, T. Ido, M. Hamabe, M. Fujiwara, A. Iiyoshi, S. Morimoto, T. Bigelow and Y.P. Zhao,
Steady State Heating Technology Development for LHD; Oct. 1998
(IAEA-CN-69/FTP/21)

NIFS-565 A. Sagara, K.Y. Watanabe, K. Yamazaki, O. Motojima, M. Fujiwara, O. Mitarai, S. Imagawa, H. Yamanishi, H. Chikaraishi, A. Kohyama, H. Matsui, T. Muroga, T. Noda, N. Ohyabu, T. Satow, A.A. Shishkin, S. Tanaka, T. Terai and T. Uda,
LHD-Type Compact Helical Reactors; Oct. 1998
(IAEA-CN-69/FTP/03(R)

NIFS-566 N. Nakajima, J. Chen, K. Ichiguchi and M. Okamoto,
Global Mode Analysis of Ideal MHD Modes in L=2 Heliotron/Torsatron Systems; Oct. 1998
(IAEA-CN-69/THP1/08)

NIFS-567 K Ida, M Osakabe, K. Tanaka, T Minami, S Nishimura, S Okamura, A Fujisawa, Y Yoshimura, S Kubo, R Akiyama, D S Darrow, H Idei, H Iguchi, M Isobe, S Kado, T Kondo, S Lee, K Matsuoka, S Morita, I. Nomura, S Ohdachi, M Sasao, A Shimizu, K. Tumori, S Takayama, M Takechi, S Takagi, C Takahashi, K Toi and T. Watari,
Transition from L Mode to High Ion Temperature Mode in CHS Heliotron/Torsatron Plasmas; Oct 1998
(IAEA-CN-69/EX2/2)

NIFS-568 S Okamura, K Matsuoka, R Akiyama, D S Darrow, A Ejiri, A Fujisawa, M Fujiwara, M. Goto, K Ida H Idei, H Iguchi, N Inoue, M Isobe, K Itoh, S. Kado, K Khlopenkov, T Kondo, S Kubo, A Lazaros, S Lee, G Matsunaga, T Minami, S Morita, S Murakami, N Nakajima, N Nikai, S Nishimura, I Nomura, S Ohdachi, K Ohkuni, M Osakabe, R Pavlichenko, B Peterson, R Sakamoto, H Sanuki, M. Sasao, A Shimizu, Y. Shirai, S Sudo, S. Takagi, C Takahashi, S. Takayama, M. Takechi, K Tanaka, K. Toi, K. Yamazaki, Y. Yoshimura and T Watari,
Confinement Physics Study in a Small Low-Aspect-Ratio Helical Device CHS; Oct 1998
(IAEA-CN-69/OV4/5)

NIFS-569 M M. Skoric, T Sato, A. Maluckov, M.S. Jovanovic,
Micro- and Macro-scale Self-organization in a Dissipative Plasma; Oct 1998

NIFS-570 T Hayashi, N. Mizuguchi, T-H. Watanabe, T. Sato and the Complexity Simulation Group,
Nonlinear Simulations of Internal Reconnection Event in Spherical Tokamak; Oct 1998
(IAEA-CN-69/TH3/3)

NIFS-571 A Iiyoshi, A. Komori, A. Ejiri, M. Emoto, H Funaba, M Goto, K Ida, H Idei, S. Inagaki, S Kado, O Kaneko, K. Kawahata, S. Kubo, R Kumazawa, S. Masuzaki, T. Minami, J. Miyazawa, T Morisaki, S Morita, S Murakami, S Muto, T Muto, Y. Nagayama, Y Nakamura, H. Nakanishi, K Narihara, K. Nishimura, N Noda, T Kobuchi, S Ohdachi, N Ohyabu, Y Oka, M. Osakabe, T. Ozaki, B.J. Peterson, A. Sagara, S. Sakakibara, R Sakamoto, H. Sasao, M. Sasao, K. Sato, M. Sato, T Seki, T. Shimozuma, M. Shoji, H. Suzuki, Y. Takeiri, K. Tanaka, K. Toi, T. Tokuzawa, K. Tsumori, I Yamada, H. Yamada, S. Yamaguchi, M. Yokoyama, K.Y.Watanabe, T. Watari, R Akiyama, H. Chikaraishi, K. Haba, S. Hamaguchi, S. Iima, S. Imagawa, N. Inoue, K Iwamoto, S. Kitagawa, Y. Kubota, J. Kodaira, R. Maekawa, T. Mito. T Nagasaka, A. Nishimura, Y. Takita, C Takahashi, K. Takahata, K. Yamauchi, H. Tamura, T. Tsuzuki, S. Yamada, N. Yanagi, H. Yonezu, Y. Hamada, K. Matsuoka, K. Murai, K Ohkubo, I Ohtake, M Okamoto, S. Sato, T Satow, S Sudo, S Tanahashi, K. Yamazaki, M. Fujiwara and O. Motojima,
An Overview of the Large Helical Device Project; Oct 1998
(IAEA-CN-69/OV1/4)

NIFS-572 M. Fujiwara, H. Yamada, A. Ejiri, M. Emoto, H. Funaba, M. Goto, K. Ida, H Idei, S. Inagaki, S. Kado, O Kaneko, K. Kawahata, A. Komori, S. Kubo, R. Kumazawa, S. Masuzaki, T. Minami, J Miyazawa, T Morisaki, S. Morita, S. Murakami, S Muto, T. Muto, Y. Nagayama, Y. Nakamura, H. Nakanishi, K. Narihara, K. Nishimura, N. Noda, T. Kobuchi, S. Ohdachi, N. Ohyabu, Y. Oka, M. Osakabe, T Ozaki, B. J. Peterson, A. Sagara, S. Sakakibara, R. Sakamoto, H. Sasao, M. Sasao, K. Sato, M. Sato, T. Seki, T. Shimozuma, M. Shoji, H. Sazuki, Y. Takeiri, K. Tanaka, K. Toi, T Tokuzawa, K. Tsumori, I. Yamada, S. Yamaguchi, M Yokoyama, K.Y. Watanabe, T. Watari, R Akiyama, H. Chikaraishi, K. Haba, S. Hamaguchi, M Iima, S. Imagawa, N Inoue, K Iwamoto, S. Kitagawa, Y. Kubota, J. Kodaira, R. Maekawa, T. Mito, T. Nagasaka, A. Nishimura, Y. Takita, C. Takahashi, K Takahata, K. Yamauchi, H. Tamura, T. Tsuzuki, S. Yamada, N. Yanagi, H. Yonezu, Y. Hamada, K. Matsuoka, K. Murai, K. Ohkubo, I Ohtake, M. Okamoto, S. Sato, T. Satow, S. Sudo, S Tanahashi, K. Yamazaki, O. Motojima and A. Iiyoshi,
Plasma Confinement Studies in LHD; Oct. 1998
(IAEA-CN-69/EX2/3)

NIFS-573 O. Motojima, K. Akaishi, H Chikaraishi, H. Funaba, S Hamaguchi, S. Imagawa, S. Inagaki, N Inoue, A. Iwamoto, S. Kitagawa, A. Komori, Y. Kubota, R. Maekawa, S. Masuzaki, T. Mito, J Miyazawa, T. Morisaki, T. Muroga, T. Nagasaka, Y. Nakmura, A Nishimura, K. Nishimura, N. Noda, N. Ohyabu, S. Sagara, S. Sakakibara, R. Sakamoto, S. Satoh, T. Satow, M. Shoji, H. Suzuki, K Takahata, H. Tamura, K. Watanabe, H. Yamada, S. Yamada, S. Yamaguchi, K. Yamazaki, N. Yanagi, T. Baba, H. Hayashi, M Iima, T. Inoue, S Kato, T. Kato, T. Kondo, S. Moriuchi, H. Ogawa, I. Ohtake, K Ooba, H. Sekiguchi, N. Suzuki, S Takami, Y. Taniguchi, T Tsuzuki, N Yamamoto, K Yasui, H. Yonezu, M. Fujiwara and A Iiyoshi,
Progress Summary of LHD Engineering Design and Construction; Oct 1998
(IAEA-CN-69/FT2/1)

NIFS-574 K. Toi, M. Takechi, S. Takagi, G. Matsunaga, M. Isobe, T. Kondo, M. Sasao, D.S. Darrow, K. Ohkuni, S. Ohdachi, R. Akiyama A. Fujisawa, M Gotoh, H. Idei, K. Ida, H. Iguchi, S. Kado, M. Kojima, S Kubo, S. Lee, K. Matsuoka, T Minami, S. Morita, N. Nikai, S. Nishimura, S. Okamura, M. Osakabe, A. Shimizu, Y. Shirai, C Takahashi, K. Tanaka, T Watari and Y. Yoshimura,
Global MHD Modes Excited by Energetic Ions in Heliotron/Torsatron Plasmas; Oct. 1998
(IAEA-CN-69/EXP1/19)

NIFS-575 Y. Hamada, A. Nishizawa, Y Kawasumi, A Fujisawa, M. Kojima, K Narihara, K. Ida, A. Ejiri, S. Ohdachi, K Kawahata, K. Toi, K. Sato, T. Seki, H. Iguchi, K. Adachi, S. Hidekuma, S Hirokura, K. Iwasaki, T. Ido, R Kumazawa, H. Kuramoto, T. Minami, I. Nomura, M. Sasao, K.N. Sato, T Tsuzuki, I Yamada and T. Watari,
Potential Turbulence in Tokamak Plasmas; Oct. 1998
(IAEA-CN-69/EXP2/14)

NIFS-576 S. Murakami, U. Gasparino, H. Idei, S. Kubo, H. Maassberg, N. Marushchenko, N. Nakajima, M. Romé and M. Okamoto,
5D Simulation Study of Suprathermal Electron Transport in Non-Axisymmetric Plasmas; Oct. 1998
(IAEA-CN-69/THP1/01)

NIFS-577 S. Fujiwara and T Sato,
Molecular Dynamics Simulation of Structure Formation of Short Chain Molecules; Nov. 1998

NIFS-578 T. Yamagishi,
Eigenfunctions for Vlasov Equation in Multi-species Plasmas Nov. 1998

NIFS-579 M. Tanaka, A. Yu Grosberg and T. Tanaka,
Molecular Dynamics of Strongly-Coupled Multichain Coulomb Polymers in Pure and Salt Aqueous Solutions; Nov. 1998

NIFS-580 J. Chen, N. Nakajima and M. Okamoto,
Global Mode Analysis of Ideal MHD Modes in a Heliotron/Torsatron System: I. Mercier-unstable Equilibria; Dec. 1998

NIFS-581 M. Tanaka, A. Yu Grosberg and T. Tanaka,
Comparison of Multichain Coulomb Polymers in Isolated and Periodic Systems: Molecular Dynamics Study; Jan. 1999

NIFS-582 V.S. Chan and S. Murakami,
Self-Consistent Electric Field Effect on Electron Transport of ECH Plasmas; Feb. 1999

NIFS-583 M. Yokoyama, N. Nakajima, M. Okamoto, Y. Nakamura and M. Wakatani,
Roles of Bumpy Field on Collisionless Particle Confinement in Helical-Axis Heliotrons; Feb. 1999

NIFS-584 T.-H. Watanabe, T. Hayashi, T. Sato, M. Yamada and H. Ji,
Modeling of Magnetic Island Formation in Magnetic Reconnection Experiment; Feb. 1999

NIFS-585 R. Kumazawa, T. Mutoh, T. Seki, F. Shinpo, G. Nomura, T. Ido, T. Watari, Jean-Marie Noterdaeme and Yangping Zhao,
Liquid Stub Tuner for Ion Cyclotron Heating; Mar 1999

NIFS-586 A. Sagara, M. Iima, S. Inagaki, N. Inoue, H. Suzuki, K. Tsuzuki, S. Masuzaki, J. Miyazawa, S. Morita, Y Nakamura, N. Noda, B. Peterson, S Sakakibara, T. Shimozuma, H. Yamada, K. Akaishi, H. Chikaraishi, H. Funaba, O Kaneko, K. Kawahata, A. Komori, N. Ohyabu, O. Motojima, LHD Exp. Group 1, LHD Exp. Group 2,
Wall Conditioning at the Starting Phase of LHD; Mar. 1999

NIFS-587 T. Nakamura and T. Yabe,
Cubic Interpolated Propagation Scheme for Solving the Hyper-Dimensional Vlasov-Poisson Equation in Phase Space; Mar 1999

NIFS-588 W.X. Wnag, N. Nakajima, S. Murakami and M. Okamoto,
An Accurate δf Method for Neoclassical Transport Calculation; Mar. 1999

NIFS-589 K. Kishida, K. Araki, S. Kishiba and K. Suzuki,
Local or Nonlocal? Orthonormal Divergence-free Wavelet Analysis of Nonlinear Interactions in Turbulence; Mar. 1999

NIFS-590 K. Araki, K. Suzuki, K. Kishida and S. Kishiba,
Multiresolution Approximation of the Vector Fields on T^3; Mar. 1999

NIFS-591 K. Yamazaki, H. Yamada, K.Y.Watanabe, K. Nishimura, S. Yamaguchi, H. Nakanishi, A. Komori, H. Suzuki, T. Mito, H. Chikaraishi, K. Murai, O. Motojima and the LHD Group,
Overview of the Large Helical Device (LHD) Control System and Its First Operation; Apr. 1999

NIFS-592 T. Takahashi and Y. Nakao,
Thermonuclear Reactivity of D-T Fusion Plasma with Spin-Polarized Fuel; Apr 1999

NIFS-593 H. Sugama,
Damping of Toroidal Ion Temperature Gradient Modes; Apr. 1999

NIFS-594 Xiaodong Li,
Analysis of Crowbar Action of High Voltage DC Power Supply in the LHD ICRF System; Apr. 1999

NIFS-595 K. Nishimura, R. Horiuchi and T. Sato,
Drift-kink Instability Induced by Beam Ions in Field-reversed Configurations; Apr. 1999

NIFS-596 Y. Suzuki, T-H. Watanabe, T. Sato and T. Hayashi,
Three-dimensional Simulation Study of Compact Toroid Plasmoid Injection into Magnetized Plasmas; Apr. 1999